Alkylphosphocholine Analogs for Broad Spectrum Cancer Imaging and Therapy

Jamey P. Weichert[1,3,5,6]*, Paul A. Clark[2], Irawati K. Kandela[6], Abram M. Vaccaro[6], William Clarke[6], Marc A. Longino[1,6], Anatoly N. Pinchuk[1,6], Mohammed Farhoud[5], Kyle I. Swanson[2], John M. Floberg[3], Joseph Grudzinski[3,6], Benjamin Titz[6], Anne M. Traynor[4], Hong-En Chen[2], Lance T. Hall[1], Christopher J. Pazoles[6], Perry J. Pickhardt[1], John S. Kuo[2,5]*

[1] Department of Radiology, University of Wisconsin School of Medicine and Public Health, Madison, Wisconsin 53792, USA

[2] Department of Neurological Surgery, University of Wisconsin School of Medicine and Public Health, Madison, Wisconsin 53792, USA

[3] Department of Medical Physics, University of Wisconsin School of Medicine and Public Health, Madison, Wisconsin 53792, USA

[4] Department of Medicine, University of Wisconsin School of Medicine and Public Health, Madison, Wisconsin 53792, USA

[5] Carbone Cancer Center, University of Wisconsin School of Medicine and Public Health, Madison, Wisconsin, 53792, USA

[6] Cellectar Biosciences, Inc, 3301 Agriculture Drive, Madison, Wisconsin 53716, USA.

* Corresponding authors: jweichert@uwhealth.org (J.P.W.); j.kuo@neurosurgery.wisc.edu (J.S.K.)

One sentence summary: Tumor-specific alkylphosphocholine analogs were evaluated as imaging and therapy agents in patients and in animal models of human cancer.

Abstract

Many solid tumors contain an over-abundance of phospholipid ethers relative to normal cells. Capitalizing on this difference, we created cancer-targeted alkylphosphocholine (APC) analogs through structure activity analyses. Depending on the iodine isotope

used, radioiodinated APC analog CLR1404 was used as either a PET imaging (^{124}I) or molecular radiotherapeutic (^{131}I) agent. CLR1404 analogs displayed prolonged tumor-selective retention in 55 in vivo rodent and human cancer and cancer stem cell models. ^{131}I-CLR1404 also displayed efficacy (tumor growth suppression, survival extension) in a wide range of human tumor xenograft models. Human PET/CT and SPECT/CT imaging in advanced cancer patients with ^{124}I- or ^{131}I-CLR1404, respectively, demonstrated selective uptake and prolonged retention in both primary and metastatic malignant tumors. Combined application of these chemically identical APC-based radioisosteres will enable personalized dual modality cancer therapy of using molecular ^{124}I-CLR1404 tumor imaging for planning ^{131}I-CLR1404 therapy.

Introduction

Selective delivery of diagnostic imaging and therapy agents to malignant tumors while sparing healthy tissues continues to be the major goal in cancer research and in clinical practice. Approaches to achieve this goal are reflected in therapeutic agents that are already approved or in development. Tumor-targeting vehicles based on antibodies, viruses, peptides, and nanoparticles have been used to deliver a wide range of "payloads" to cancer cells, including radioactive isotopes, imaging agents, oncolytic viruses, metals, and chemotherapeutic drugs (*1-8*). Currently available cancer therapy modalities offer either broad applicability across cancer types (e.g. external beam radiation, surgery, cytotoxic drugs) or cancer selectivity based on higher expression of drug targets (genes) in cancer cell sub-populations compared to normal cells (e.g. *PML-RARα, BCR-ABL, c-kit, EGFR, ERBB2/Her2/neu*). Still, many cancers recur despite the initial disease control and therapeutic efficacy of many available cancer therapies. Recent evidence suggests that cancer recurrence likely involves failure to eradicate cancer cells that are relatively resistant to current therapies, such as cancer stem cells (or cancer stem-like cells) (*9-11*).

A new therapeutic modality that minimizes damage to normal cells, and combines cancer selectivity (including cancer stem cells) with a broad anticancer mechanism would represent a paradigm shift in cancer treatment. Naturally occurring phospholipid ethers (PLE) selectively accumulate in human cancer cells compared to normal cells (*12-14*). We have previously examined the structure activity relationships for radioiodinated aryl PLE and a subset of alkylphosphocholine (APC) derivatives to see how alterations in molecular structure affected tumor retention of these compounds (*15-18*). These studies indicated that, for glycerol-derived PLE analogs, the stereochemistry at the *sn*-2 position of glycerol did not affect tumor uptake and retention in a rat sarcoma model. The length of the hydrophobic alkyl chain was discovered as another key

characteristic that affected tumor retention of these compounds. Decreasing the alkyl chain length from 12 carbons (C12) to C7 resulted in little or no tumor accumulation, whereas increasing the chain length had the opposite effect, with C15 and C18 analogs showing delayed plasma clearance and enhanced tumor uptake. Furthermore, in the C12 APC series, substitution of the choline part of the molecule with ethanol, ethanolamine, or 3,3-dimethyl-1-butanol reduced tumor uptake. From these studies, we found that the glycerol backbone was not required for tumor avidity, the alkyl chain must contain >11 methylene groups, and the position of iodine on the phenyl ring did not influence tumor uptake or specificity.

Ultimately, CLR1404 [18-(*p*-iodophenyl) octadecylphosphocholine] was identified among 9 PLE and APC analogs as the best tumor-imaging agent in rodent models (*18*). In follow-up pharmacologic toxicology studies, CLR1404 additionally exhibited low rodent toxicity and lower liver, kidney, bladder, and abdominal exposure compared to other derivatives. Moreover, replacement of iodine with optically active moieties yielded similar tumor selectivity and retention, suggesting bulk structural tolerance in that location. Therefore, we hypothesized that the CLR1404 chemical scaffold (Fig. 1) is uniquely well-suited to deliver radioiodine isotopes and other reporters that are useful for either diagnostic imaging or therapy for a broad spectrum of solid tumors.

Unlike classical DNA-targeted cytotoxic agents, alkylphospholipids, including APC, target cellular and intracellular membranes (*19*). When administered at therapeutic doses, alkylphospholipids inhibit phosphatidylcholine biosynthesis, interfere with lipid transduction pathways, and block the endoplasmic reticular transport of cholesterol, thereby ultimately disrupting cholesterol homeostasis and membrane lipid raft function (*20*). Lipid rafts are specialized plasma membrane microdomains rich in cholesterol and sphingomyelin (*21*), which spatially organize signaling pathways and regulate cell proliferation and survival (apoptosis) (*22*). Lipid rafts, which are more abundant in cancer cells relative to normal cells (*23*), serve as cellular portals of entry for CLR1404 and other alkylphospholipids into tumors.

Here, we report results of in vitro and in vivo testing with radioisotope-labeled CLR1404 for diagnostic imaging (^{124}I-CLR1404) and for cancer therapy (^{131}I-CLR1404), as well as imaging data with the fluorescent analog CLR1501, in a wide variety of tumor models. We also present first-in-human imaging results that show CLR1404 has tumor targeting and retention properties in cancer patients. CLR1404 represents a new class of

synthetic APC analogs to be used for broad spectrum, tumor-selective molecular imaging and therapy agents in human cancers.

RESULTS

CLR1404 analogs are preferentially taken up and retained in cancer cell lines

CLR1501, a fluorescently labeled CLR1404 analog (Fig. 1), was administered to 7 different cancer cell lines (renal, colorectal, glioma, ovarian, pancreatic, melanoma, and prostate) and a normal human skin fibroblast line in vitro. Confocal microscopy 24 hours later showed that CLR1501 exhibited 5- to 9-fold preferential uptake in these cancer cell lines in vitro compared to normal fibroblasts (Fig. 2A and fig. S1). Retained CLR1501 was associated with plasma and organelle membranes. Cancer-selective localization of alkylphosphocholine analogs was also observed in a co-culture of human prostate carcinoma cells (PC-3) and a primary normal human skin fibroblast cell line treated with CLR1501 for 24 hours and imaged with confocal microscopy (Fig. 2B).

To further examine cancer cell-selective targeting, three pairs of patient-matched normal and cancer cell lines were treated with ^{125}I-CLR1404. The osteosarcoma cell line 704.T is from the same patient as the normal skin cell line, 704.sk. There was a 2.8-fold increase in the observed ^{125}I-CLR1404 uptake by the osteosarcoma cell line compared to normal, patient-matched cells (Fig. 2C). Similarly, for two non-small cell lung cancer (NSCLC) patient cell lines, H2122 and H1395, there were significant increases in ^{125}I-CLR1404 uptake compared to their patient-matched normal cell lines BL2122 and BL1395 (derived from their respective B-lymphoblast cell lines), respectively.

Next we visualized the kinetics of CLR1501 entry into PC-3 cells over the course of 1 hour. CLR1501 entered cells via plasma membranes and collected in membrane-bound vesicles, eventually localizing to membranes of cytoplasmic organelles (movie S1). Maximal uptake of ^{125}I-CLR1404 was reached after 48 hours in normal skin fibroblasts compared with 24 hours in human NSCLC cells, with the final levels of ^{125}I-CLR1404 uptake approximately 4-fold higher than observed in normal cells (fig. S2).

Pretreatment of PC-3 cells with Filipin III, an agent that sequesters cholesterol and disrupts lipid rafts, resulted in nearly 40% less uptake of ^{125}I-CLR1404 compared to untreated control cells (fig. S3). This supports the hypothesis that CLR1404 uses lipid rafts as portals of entry into cancer cells

Because of their emerging role in cancer progression and relapse, cancer stem cells were also analyzed for CLR1404 uptake. Human glioblastoma (GBM) stem-like cell

(GSC) lines were isolated from patient surgical specimens. Six GSC lines (12.1, 22, 33, 44, 99, 105) were validated for enhanced expression of stem cell markers [cluster of differentiation 133 (CD133) and nestin] and multi-lineage potential (neuronal and glial) (*11, 24*). Patient-matched, serum-cultured GBM cell lines (serGBM) 22, 33, and 99 were established from the same specimens used for establishing the GSC lines. Stem-like properties of GSCs are rapidly lost in serum culture, so serGBM lines served as a model of non-GSC GBM cells. Both GSC and serum-cultured GBM cells exhibited enhanced CLR1501 uptake compared to normal human astrocytes and fetal human neural stem cell lines (NSCs) (Fig. 3, A and B). Flow cytometry confirmed greater uptake for GSC and serGBM lines compared to astrocytes (Fig. 3B).

Although enriched for GSCs, glioblastoma spheres consist of a mixture of GSCs as well as non-GSCs. Therefore we sought to further verify that GSCs are labeled with CLR1404 analogs by co-labeling with the GSC marker CD133. CLR1501 uptake was seen in both $CD133^+$ and $CD133^-$ GSCs; however, significantly higher fluorescence was found in $CD133^+$ GSCs compared to $CD133^+$ NSCs (Fig. 3C and fig. S4). These data indicate that APC analogs preferentially label all GBM cells, including cancer stem-like cells, with minimal retention by normal neural and neural stem cells.

APC analogs undergo selective uptake and retention in tumors

Radioiodinated ^{124}I-CLR1404 was tested in subcutaneous and orthotopic xenografts of 57 different spontaneous, transgenic, human and rodent malignant cell lines and tumor types. Following intravenous administration, ^{124}I-CLR1404 localized in almost all primary and metastatic malignant tumors regardless of anatomic location (table S1). Representative examples are of both human (Fig. 4A) and rodent (Fig. 4B) tumors. Pronounced and sustained tumor accumulation was seen by 24 hours in a human prostate cancer xenograft (PC-3), with continued clearance from healthy tissue evident between 48 and 120 hours (fig. S5A). Although liver metastases from all other cancer types were successfully visualized, flank xenografts of two human hepatocellular carcinoma lines did not show prolonged retention (table S1).

In vivo cancer stem cell labeling with CLR1501 was also demonstrated in GSC-derived orthotopic xenografts in mice. After MRI-verification of brain tumor, CLR1501 administered intravenously labeled all tumor cells (Fig. 5, A and B), including GSCs that stained positive for nestin, Olig2, and CD15/SSEA-1 (Fig. 5, C to E. These results were verified using *ex vivo* flow cytometry analysis of CD133 expression in glioblastoma

xenograft cells. Sub-populations of $CD133^+$ glioma cells (2-26%) were detected in the xenografts of three distinct human-derived glioblastoma lines (U251 glioma, 22 GSC, and 105 GSC). A high fraction of $CD133^+$ glioblastoma cells were co-labeled with CLR1501 (Fig. 5, F and G). It is important to note that a small percentage of $CD133^+$ cells may be retained in the serum-cultured U251 glioma line (*25*), and that serum-cultured tumor lines may re-express CD133 after in vivo engraftment (*26*). Therefore, the presence of $CD133^+$ U251 cells within mouse brain tumor xenografts is not unexpected.
Benign or premalignant tumors showed very little or no uptake in animal models (Table S1). Moreover, unlike ^{18}F-fluorodeoxyglucose (FDG), a common PET agent for tumor imaging, CLR1404 analogs were not seen in either inflammatory (fig. S5B) or premalignant lesions (table S1). Mean inflammatory lesion to tumor ratio was 4.94 with FDG and 0.34 for CLR1404. Using non-invasive dual-modality PET-CT colonoscopy and ^{124}I-CLR1404, we visualized both premalignant colonic adenomatous polyps and malignant adenocarcinomas that spontaneously develop in a Pirc rat model (fig. S6). Three-dimensional micro-PET/CT scanning performed 24 h post-intravenous injection of ^{124}I-CLR1404 revealed PET enhancement of one histologically confirmed malignant adenocarcinoma, but little or no uptake in 19 coexisting premalignant adenomas (movie S2).

Radiotherapy with ^{131}I-CLR1404 in human tumor xenograft rodent models

Owing to observed selective uptake into cancer cells compared to normal cells, coupled with the well-established efficacy of ^{131}I-based molecular radiotherapy in multiple cancer types [such as thyroid cancer, neuroblastoma, non-Hodgkin's lymphoma, hepatocellular carcinoma (*27-29*)], ^{131}I-CLR1404 was evaluated in human tumor xenograft models of clear cell renal carcinoma (Caki-2), colorectal carcinoma (HCT-116), ovarian adenocarcinoma (Ovcar-3), triple negative breast adenocarcinoma (MDA-MB-231), uterine sarcoma (MES-SA/Dx5), glioma (U87-MG), pancreatic carcinoma (Mia Paca-2) and prostate carcinoma (PC-3). A single, non-optimized IV dose of 100-145 μCi of ^{131}I-CLR1404 was sufficient to provide statistically significant tumor growth suppression and survival benefit in these cancer models when compared to control animals treated with an equivalent mass dose of non-radioactive CLR1404. Antitumor efficacy was pronounced in terms of the degree and duration of growth suppression in the renal, colorectal, ovarian, prostate, and triple-negative breast cancer models (Fig. 6). In the relatively radioresistant uterine sarcoma and glioma models, two injections of ^{131}I-

CLR1404 on days 0 and 20 or 0 and 7, respectively, prevented tumor growth and prolonged survival (fig. S7). These data suggest that tumor delivery of therapeutic ^{131}I with CLR1404 afforded survival benefit in most tumor models following a single treatment.

Tumor imaging with ^{124}I- and ^{131}I-CLR1404 in human cancer patients

After successful imaging and therapy in rodent models of human cancer, we started human trials of PET/CT imaging with CLR1404. Preliminary results in a NSCLC patient without neurological symptoms using ^{124}I-CLR1404 PET/CT show three previously unknown brain lesions highly suspicious for metastases, subsequently confirmed with gadolinium-enhanced MRI, and altered clinical management to include brain radiotherapy (Fig. 7A). Moreover, although primary brain tumors were visualized with MRI (Fig. 7, B and C), high tumor-to-normal brain ratios following administration of ^{124}I-CLR1404 also permitted easy tumor visualization; for example, a tumor/brain ratio of 30 on PET obtained 2 days after injection of 5 mCi of ^{124}I-CLR1404 into a patient with grade III astrocytoma (fig. S8). Tumor uptake and prolonged retention was also demonstrated using SPECT/CT imaging in a colorectal cancer patient with known liver and lung metastases 21 days after injection of ^{131}I-CLR1404 (fig. S9).

We also successfully isolated and expanded GSCs (line 107) from a surgical GBM specimen obtained after preoperative ^{124}I-CLR1404 injection (Fig. 7, B to D). After implantation of 107 GSCs into immunodeficient mice, resultant tumor xenografts were visualized *ex vivo* using CLR1502 (near-infrared CLR1404 analog) (Fig. 7E). Highly invasive glioma xenograft phenotypes were also verified after histological processing (Fig. 7, F to I).

DISCUSSION

We demonstrate in vitro and in vivo selective uptake of APC-based imaging and therapeutic agents by a wide range of malignant cells. For in vivo studies, both rodent cancer models and human patients were studied using analogs containing either a PET-imaging isotope (^{124}I) or a SPECT-imaging, therapeutic isotope (^{131}I). The cancer cell-selective targeting properties of CLR1404 make it an ideal candidate for both diagnostic and therapeutic applications, thereby illustrating the tandem imaging and therapy paradigm for this versatile APC-based chemical scaffold. As a cancer drug delivery vehicle, its broad-spectrum applicability represents an advance over other more narrowly

targeted delivery mechanisms, such as antibodies and peptides. Furthermore, in the case of structurally identical ^{124}I-CLR1404 and ^{131}I-CLR1404, it represents a perfectly matched diagnostic/therapeutic pairing for personalizing and optimizing cancer therapy - with ^{124}I-CLR1404 serving in the diagnostic/imaging capacity for predicting, planning and following the potential therapeutic efficacy of ^{131}I-CLR1404. Similar to radioiodinated CLR1404 analogs, the fluorescent derivative, CLR1501, also displayed selective uptake and retention in various human cancer cell lines in vitro and in malignant tumors in vivo compared to normal human cells or tissues.

Uptake of the CLR1404 chemical scaffold into cancer cells appears to partially involve interaction with lipid raft regions of the plasma membrane (*22, 30-32*). This hypothesis was supported in this study by decreased uptake of ^{125}I-CLR1404 after pre-treatment of human cancer cells with the lipid raft disruptor, filipin III. A lipid raft-based mechanism for uptake into cancer cells has also been reported for other alkylphospholipids (*21*). Importantly, lipid rafts and cholesterol (a key raft constituent) are more abundant in cancer cells compared to normal cells (*23*), and may partially account for CLR1404's cancer cell selectivity. CLR1404 interaction with lipid rafts may also explain the finding that CLR1404 uptake was significantly higher in CD133^{+} GSCs versus matched CD133^{-} non-GSCs (in 4 out of 5 sphere-cultured lines); because CD133 was demonstrated to localize to cholesterol-rich lipid raft microdomains (*33*).

PET/CT imaging of a wide range of in vivo rodent cancer models using CLR1404 derivatives showed cancer-selective uptake and retention. Notably, these models include genetically engineered tumors and spontaneous tumors, in addition to human tumor xenograft models (subcutaneous and orthotopic). Exploiting the sensitivity and quantification properties of PET, ^{124}I-CLR1404 imaging revealed both primary cancers and metastatic lesions in these models. Malignant tumor selectivity was confirmed in tissue distribution studies with ^{125}I-CLR1404 in multiple animal tumor models (*18*).

Initial imaging results obtained with ^{124}I-CLR1404 in a small number of human lung and brain cancer patients confirmed tumor uptake and retention properties seen in preclinical models. Tumor conspicuity was particularly striking due to the combination of high brain tumor uptake (primary gliomas and brain metastases) and low normal brain background radioactivity. ^{124}I-CLR1404 holds promise as a broadly applicable diagnostic PET imaging tool with widespread oncology indications. In addition to its potential utility for detecting and staging cancer (including total tumor burden and metastases), the 4-day radioactive half-life of ^{124}I-CLR1404 may enable early post-operative PET imaging to

detect and quantitate any remaining tumor cells after resections. Furthermore, ^{124}I-CLR1404 may offer several important advantages over the current state-of-the-art oncology PET imaging agent, ^{18}F-FDG. These may include greater specificity for cancer cells (FDG accumulates in all tissues that metabolize glucose at a relatively high rate, including tumors, inflammation and normal brain), application to a broader range of cancer types, and logistical advantages due to a substantially longer radioactive half-life (^{124}I-CLR1404 = 4 days vs. ^{18}F-FDG = 110 minutes).

The versatility of the APC-based chemical scaffold was further illustrated by the therapeutic ^{131}I-CLR1404 radioisostere. ^{131}I is a well-established cytotoxic radioisotope. Treatment efficacy, measured as tumor growth suppression and survival extension, was demonstrated in a wide range of human tumor xenograft models, some after only a single i.v. dose. Patient data showed preferential uptake and prolonged tumor retention of ^{131}I-CLR1404 compared to surrounding normal tissues (including bone marrow). Thus, ^{131}I-CLR1404 combines a powerful and widely applicable therapeutic modality (radiation) with a broad spectrum cancer targeting mechanism.

There are still many important questions to answer for a better understanding and optimal translation of these APC analogs to clinical use. Cancer and cancer stem cell-specific uptake and retention of CLR1404 analogs in many other cancer types need to be verified, beyond the GSC and GBM data in this study. Significant for CNS tumor therapy, the blood-brain barrier (BBB) permeability of CLR1404 analogs remains unknown. Primary or metastatic brain tumors often alter BBB permeability and other vascular properties (*34*), which may enhance the permeability of CLR1404 analogs. Minimal uptake and retention in normal brain both in animal models and in humans suggests a low CLR1404 analog permeability across intact BBB; alternatively, normal neural tissues may also metabolize CLR1404 analogs more rapidly than other body tissues. Pathological correlation of tumor tissue with ^{124}I-CLR1404 imaging signal is also being tested in an ongoing glioma imaging clinical trial (www.clinicaltrials.gov, NCT01898273).

Optimal dosing and imaging parameters for human imaging and therapy for different cancers (i.e. primary versus metastatic, body versus brain tumors), and relative to patient weight, age or other physical parameters continue to be investigated in ongoing and proposed clinical trials. The potential use of optical CLR1404 analogs in intraoperative applications is also being vigorously pursued for clinical trial validation with multiple cancers. Other applications with important clinical potential exploits the

cancer cell-specific detection of CLR1404 analogs. CLR1404 imaging may be used to evaluate the efficacy of cancer therapies, and to determine tumor recurrence versus pseudoprogression, a difficult task with current imaging technologies.

In conclusion, the alkylphosphocholine analog-based scaffold exemplified by CLR1404 can act as a cancer and cancer stem cell-targeted vehicle for diagnosis and therapy in a wide range of malignant tumor types. Further clinical trial validation and determination of optimal human dosing and imaging parameters of radiolabeled and optical CLR1404 analogs are continuing for translation to clinical use in multiple cancers. Potential use in determining therapeutic efficacy and tumor recurrence versus pseudoprogression are also being explored for these versatile agents.

Materials and Methods

Study design

Our goal was to evaluate the use of CLR1404 APC analogs in tumor imaging and therapy. We tested radioiodinated and fluorescent CLR1404 analogs (Fig. 1) for tumor-specific labeling and retention properties in vitro and in vivo in 57 different tumor cell lines and xenograft and transgenic tumor models, and also tested whether tumor labeling is altered by lipid raft disruption. Using 6 distinct human GSC lines, we tested the ability of APC analogs to label both cancer stem cells and serum-cultured, non-stem cells from GBM**.** Then we showed the efficacy of ^{131}I-CLR1404 therapy in animal tumor models of 8 different human cancers. We also evaluated the use of APC analogs in human cancer imaging in adult patients with different types of primary and metastatic cancers throughout the body and brain through the following clinical trials registered on clinicaltrials.gov: NCT01516905, NCT01540513, NCT01495663, NCT00582283, NCT01898273.

Synthesis and radioiodination of CLR1404

Synthesis of 18-(*p*-iodophenyl)octadecyl phosphocholine was previously reported (*18*). Radioiodination was achieved in 70% isolated radiochemical yield via isotope exchange with ^{124}I (IBA Molecular North America), ^{125}I- or ^{131}I -sodium iodide (Perkin-Elmer) (*35*). Following purification (>99% radiochemical purity) and accurate mass quantification by HPLC [normal phase, isocratic isopropanol/hexanes/water (13:10:2)], the radiopharmaceutical was dissolved in absolute ethanol (50-500 μl) and Tween-20 (0.1 μl/μg of compound). The ethanol was removed under vacuum and the residue dissolved

in sterile water to give a final solution containing no more than 0.4% Tween-20. Sterilization is achieved by filtration through a sterile 0.2-μm filter unit. Injection solutions are tested for pyrogens using the Limulus Amebocyte Lysate test kit. Synthesis of the other analogs, CLR1501 and CLR1502, is shown in fig. S10 and described in Supplementary Methods.

Cell culture

Human cancer cell lines were purchased from American Type Culture Collection (ATCC). They included: Caki-2 (renal; clear cell carcinoma), HCT-116 (colorectal carcinoma); MES-SA/Dx5 (uterine sarcoma) [all maintained in McCoy's 5a media supplemented with 10% fetal bovine serum (FBS)], Ovcar-3 (ovarian adenocarcinoma) [maintained in RPMI media supplemented with 20% FBS], U87-MG (glioma) [maintained in MEM media supplemented with 10% FBS], Mia Paca-2 (pancreatic carcinoma) [maintained in Dulbecco's Modified Eagle's media supplemented with 10% fetal bovine serum], PC-3 (prostate carcinoma) [maintained in F-12K media supplemented with 10% FBS], MDA-MB-231 (triple negative mammary gland adenocarcinoma) [maintained in Leibovitz's media supplemented with 10% FBS], A549 (non-small cell lung carcinoma) [maintained in F-12 media supplemented with 10% FBS]. Normal human skin fibroblasts were purchased from ATCC and grown in Fibroblast Basal Medium PCS-201-030 supplemented with serum-free kit (Fibroblast Growth Kit–Serum-free PCS-201-040). All media (except for MDA-MB-231 cell line) also contained 100 U/ml Penicillin and 100 μg/ml streptomycin and were maintained at 37^{o}C with 5% CO_2 in air.

Fluorescent staining and confocal imaging

All cells were maintained at 37°C in appropriate media supplemented with 10% FBS and 5% CO_2. Before imaging, the cells were removed from flasks with 0.25% trypsin and were allowed to grow overnight on the microslides VI (Ibidi). The next day, the cells were washed with phosphate-buffered saline (PBS) and the cells were incubated with either 5 or 7.5 μM (as indicated) of CLR1501 in appropriate serum-free media for 24 hours. CLR1501 was formulated with 0.4% of Polysorbate 20, 2% of ethanol and saline. After washing thoroughly with PBS, the cells were imaged using Bio-Rad Radiance 2100 MP Rainbow laser scanning/multiphoton confocal microscope using a 1 second exposure time. Alternatively, cells were visualized using a Nikon A1R confocal microscope (Keck

Laboratory, University of Wisconsin-Madison). The emission signal of CLR1501 was detected using Alexa Fluor 488 filters (ex/em 480/520 nm).

Cell culture videography

PC-3 cells, a human prostate adenocarcinoma, were maintained in F12 media supplemented with 10% FBS and 1% Penicillin and Streptomycin. The cells were plated overnight in Matek petri dish. The next day the cells were washed with PBS and stained with Image-IT LIVE Mitochondrial and Nuclear Labeling Kit provides two stains – red-fluorescent MitoTracker Red CMXRos dye and blue-fluorescent Hoechst 33342 dye for highly selective mitochondrial and nuclear staining (Invitrogen). The image acquisition was performed with an A1R Nikon confocal system and was initiated when 5 µM CLR1501 was added to the petri dish, the video (movie S1) was acquired for 1 hour.

Matched cell lines

Three sets of normal human and cancer cell lines were purchased from American Type Culture Collection (ATCC). The lung adenocarcinoma cell line, (NCI-H1395) and a normal B-lyphoblast cell line derived from the same patient (NCI-BL1395) were both cultured in RPMI-1640 Medium supplemented with 10% fetal bovine serum. The non-small cell lung cancer cell line (NCI-H2122) and a normal B-lyphoblast cell line derived from the same patient (NCI-BL2122) were also both cultured in RPMI-1640 Medium supplemented with 10% fetal bovine serum. The osteosarcoma cell line (Hs704.T) and a normal skin fibroblast cell line derived from the same patient (Hs 704.sk) were both cultured in Dulbecco's Modified Eagle's Medium supplemented with 10% fetal bovine serum. Uptake and retention of I-125-CLR1404 at 24 hours was determined as described above.

Isolation of glioblastoma stem-like cells (GSCs)

GSCs were isolated and propagated using marker neutral, serum-free sphere culture in stem cell medium following protocols previously reported (*11, 24*), under an approved Institutional Review Board (IRB) protocol. Using this methodology, we isolated and fully validated 6 GSC lines, 5 primary and 1 recurrent: 12.1 (recurrent), 22, 33, 44, 99, and 105. These different GSC lines exhibit varied molecular and biological properties (*24*). Human cortex fetal neural stem cells (NSCs) were maintained as previously described (*36*). SerGBM and normal human astrocytes were maintained in medium containing 10% fetal bovine serum.

Human tumor xenograft models

All described animal studies were performed according to animal protocols approved by Institutional Animal Care and Use Committee. Female athymic nude mice (Hsd: Athymic Nude-Foxn1nu, or Crl: NU-Foxn1nu; Charles River) approximately 4-5 weeks of age, 16-18 g (*n* = 6) were used for human tumor xenograft studies. Mice were anesthetized with isoflurane and injected subcutaneously with viable tumor cells in 100 µL Dulbecco's PBS (or, for glioma cells, 50 µL PBS) into the right flank. Inoculum sizes were 1×10^6 (for renal, ovarian, glioma, pancreatic, prostate and NSCLC models), 2×10^6 (for colorectal and uterine models), or 3×10^6 (breast).

Radiotherapy of tumor-bearing mice

Both ^{131}I-CLR1404 and the control, CLR1404, were formulated with 0.08% polysorbate 20 NF, 0.4% sodium ascorbate USP, 5% ethanol, 200 proof, USP in 0.9% sodium chloride injection, USP. The formulation for the glioma and breast models utilized 25% ethanol. At the time of dose preparation, the drug formulation was diluted 1:5 in 0.9% sodium chloride to reduce the ethanol concentration to approximately 5%. For assessment of CLR1404, formulation was in 0.08% of tween 20, 0.4% sodium ascorbate USP, 5% ethanol in 0.9% NaCl for injection, USP. The control was 0.9% NaCl for injection, USP. Treatment with test agents via tail vein injection (150 µL dosing volume) was initiated when tumors had reached a pre-determined size range in mm^3 (50-150 for uterine, pancreatic, glioma and breast; 50-230 for ovarian; 100-150 for NSCLC; 100-250 for renal and colorectal; 150-300 for prostate). Once tumors reached these target ranges, animals were randomly assigned to treatment groups (= Day 0).

In ^{131}I-CLR1404-treated animals, the approximate radioactivity dosed/mouse (administered on Day 0 only, unless otherwise indicated) and the number of mice/group were as follows: renal: 110 µCi, n=6; colorectal: 110 µCi, n=6; uterine: Day 0 130 µCi, Day 20 145 µCi, n=6; ovarian: 115 µCi, n=5; glioma: Days 0 and 7, 100 µCi, n=8; pancreatic: 125 µCi, n=5; prostate: Day 7 100 µCi, n=6; breast: Day 7 100 µCi, n=8-9. Control animals (n=6) were administered 0.0038 mg CLR1404 (~0.19 mg/kg, an amount equivalent to that represented by a 100 µCi dose of ^{131}I-CLR1404) on Day 0 only. In all therapy studies, mice were given potassium iodide at a concentration of 0.1% in their drinking water to block uptake of any free iodide in the drug formulation [with the addition of 0.4% w/v sweetener (Sweet and Low) to aid palatability] starting three days prior to

the estimated Day 0 for a total of 17 days. All mice were given free access to food and water throughout each study. The non-radioactive animals were housed in groups of 3-4 in cages and well separated from the radioactive animal cages. Radioactive animals were housed individually with lead shielding between cages.

Tumor growth was assessed by measuring two perpendicular tumor diameters using a caliper and the resulting measurements were used for estimating tumor volume [tumor volume = (width^2 × length × π) ÷ 6)] (*37*). Survival analysis was based on the date of death of the animal, or the date the animal was sacrificed based on either being found in moribund condition or the tumor size reaching $\geq$2000 mm^3.

In vivo micro-PET/CT imaging

Mice were anesthetized with isoflurane (2%) and scanned in a prone position on a Siemens Inveon micro-PET/CT scanner (Siemens Preclinical Systems) at various time points (ranging from 6 h to 10 days) after injection of ^{124}I-CLR1404 (80-150 µCi). CT scans were acquired with an x-ray energy of 70 kVp at 1000 mA for 200 ms with 220 degrees of rotation and 220 back-projections. CT images were reconstructed with filtered back-projection (FBP) using system software with a Shepp-Logan filter to voxel sizes of 0.2x0.2x0.2mm^3. PET scans were acquired for 10-30 minutes (40-100 million counts) and reconstructed with either 2D-OSEM with 16 subsets and 4 EM iterations or 3D-OSEM with 16 subsets and 18 iterations to voxel size of 0.8x0.8x0.8 mm^3. Corrections of normalization, dead time, scatter and attenuation were applied using the system software and the co-registered CT scan. PET data were quantified using a calibration specific to I-124. Image analysis, including region of interest (ROI quantification and co-registration of multiple time points was performed using the Inveon Research Workplace (Siemens Preclinical Systems) and Amira (Visage Imaging, Inc).

MicroPET tumor imaging with ^{124}I-CLR1404 and ^{18}F-FDG in the presence of inflammation is described in Supplementary Methods.

GSC orthotopic xenograft model

All described animal studies were performed according to animal protocols approved by Institutional Animal Care and Use Committee. GSC-derived orthotopic xenografts were initiated as previously described (*11, 24*). Cells were stereotactically injected into the right striatum of anesthetized non-obese diabetic severe combined immunodeficient (NOD-SCID) mice at the following coordinates referenced from bregma: 0 mm antero-posterior, +2.5 mm medio-lateral, and -3.5 mm dorso-ventral. Mice were than euthanized

upon tumor verification by MRI or onset of neurological symptoms, and brain processed for histological analysis.

In vivo optical studies

Fluorescent analog CLR1501 (green) or CLR1502 (near infrared) was injected (1 mg) intravenously (lateral tail vein) or retro-orbitally into anesthetized (isoflurane) mice bearing orthotopic GSC-derived xenografts. After 4 days, animals were euthanized and brains excised, fixed, frozen sectioned, and immunohistochemically stained as described above. Confocal microscopy was then performed as described above. CLR1502 was visualized using IVIS Spectrum system (Perkin-Elmer/Xenogen).

Human PET/CT imaging

Human PET brain scans were acquired on a 64-slice PET/CT scanner (Discovery VCT, General Electric) at multiple time points following the injection of approximately 5 mCi of ^{124}I-CLR1404 using a 90 minute dynamic acquisition sequence (2D, 9 frames at 10 min each, VIP list mode on) and reconstructed (Advantage work station version AW4.4, General Electric, 30 cm DFOV, 128X128, OS-EM Vue Point, 10 subsets with 2 iterations, standard Z-axis, attenuation correction and dead time, scatter, and decay correction).

SPECT/CT Images of ^{131}I-CLR1404 in Human Cancer Patients

Following the injection of ^{131}I-CLR1404, planar whole body images at multiple time points were acquired on a dual-head scanner (Infinia/Hawkeye, General Electric) using a scan speed of 10 cm/second, matrix 256 x 1024, peak set at 364 keV +/- 15% and scatter peaks of 312 keV +/- 15% and 424 keV +/- 15%, high energy all-purpose collimator, and display bone dual density. SPECT/CT images of specific regions of interest were acquired at multiple time points on a SPECT/CT scanner (Infinia/Hawkeye, General Electric) using 128 x 128 matrix, 120 projections, 3 degrees/stop, 30 s/stop, with peak set at 364 +/- 15% and scatter peaks of 312 +/- 15% and 424 +/- 15%. The CT settings are helical using a pitch of 1.9, interval 4.42 mm, voltage 140 kV, current 2.5 mA, matrix 512 x 512, filter soft and pixel 1.10 mm. Processing was performed using Volumetrix MI.

Statistics

One-way repeated measurement ANOVA (SigmaStat 3.5, Systat Software, Inc.) was performed to analyze tumor growth in control and treatment groups. A log rank statistical

analysis was used for comparison of survival benefit between groups. $p<0.05$ was considered statistically significant. Tumor growth was plotted until one animal from either group died (in order to maintain appropriate statistical analysis). Statistical analyses were performed using SigmaStat software Version 3.5. All comparisons of multiple groups were performed using one-way ANOVA analysis for variance with Bonferroni post-hoc testing. $P<0.05$ was considered significant.

Supplementary Materials

Methods

Figure S1. Preferential cancer cell uptake of CLR1501.

Figure S2. Preferential ^{125}I-CLR1404 uptake and retention in cancer cells in vitro. Figure S3. Uptake and retention of ^{125}I-CLR1404 after lipid raft disruption in prostate carcinoma cells.

Figure S4: Flow cytometry analysis of CLR1501 GSC labeling.

Figure S5. In vivo time course of biodistribution and tumor uptake of ^{124}I-CLR1404 and ^{18}F-FDG in a prostate tumor model.

Figure S6. Dual modality PET/CT virtual colonoscopy.

Figure S7. Tumor growth and animal survival after ^{131}I-CLR1404 therapy.

Figure S8. Recurrent WHO Grade III astrocytoma.

Figure S9. ^{131}I-CLR1404 SPECT/CT imaging of metastatic colorectal cancer.

Figure S10. Synthesis of optical APC analogs.

Table S1. ^{124}I-CLR1404 uptake in tumor xenografts.

Movie S1. Cellular uptake of CLR1501 in prostate cancer cells.

Movie S2. Dual modality PET/CT virtual colonoscopy in Pirc model.

REFERENCES AND NOTES

1. G. Ting, C. H. Chang, H. E. Wang, T. W. Lee, Nanotargeted radionuclides for cancer nuclear imaging and internal radiotherapy. *J Biomed Biotechnol* **2010**, (2010).
2. A. Tedcastle, R. Cawood, Y. Di, K. D. Fisher, L. W. Seymour, Virotherapy--cancer targeted pharmacology. *Drug Discov Today* **17**, 215-220 (2012).
3. M. Steiner, D. Neri, Antibody-radionuclide conjugates for cancer therapy: historical considerations and new trends. *Clin Cancer Res* **17**, 6406-6416 (2011).
4. Z. S. Guo, S. H. Thorne, D. L. Bartlett, Oncolytic virotherapy: molecular targets in tumor-selective replication and carrier cell-mediated delivery of oncolytic viruses. *Biochim Biophys Acta* **1785**, 217-231 (2008).
5. S. Kaur, G. Venktaraman, M. Jain, S. Senapati, P. K. Garg, S. K. Batra, Recent trends in antibody-based oncologic imaging. *Cancer Lett* **315**, 97-111 (2012).
6. A. Fernandez-Fernandez, R. Manchanda, A. J. McGoron, Theranostic applications of nanomaterials in cancer: drug delivery, image-guided therapy, and multifunctional platforms. *Appl Biochem Biotechnol* **165**, 1628-1651 (2011).
7. M. M. Lin, H. H. Kim, H. Kim, J. Dobson, K. Kim do, Surface activation and targeting strategies of superparamagnetic iron oxide nanoparticles in cancer-oriented diagnosis and therapy. *Nanomedicine (Lond)* **5**, 109-133 (2010).
8. S. Bhattacharyya, R. A. Kudgus, R. Bhattacharya, P. Mukherjee, Inorganic nanoparticles in cancer therapy. *Pharm Res* **28**, 237-259 (2011).

9. S. Bao, Q. Wu, R. E. McLendon, Y. Hao, Q. Shi, A. B. Hjelmeland, M. W. Dewhirst, D. D. Bigner, J. N. Rich, Glioma stem cells promote radioresistance by preferential activation of the DNA damage response. *Nature* **444**, 756-760 (2006).
10. A. Singh, J. Settleman, EMT, cancer stem cells and drug resistance: an emerging axis of evil in the war on cancer. *Oncogene* **29**, 4741-4751 (2010).
11. P. A. Clark, M. Iida, D. M. Treisman, H. Kalluri, S. Ezhilan, M. Zorniak, D. L. Wheeler, J. S. Kuo, Activation of multiple ERBB family receptors mediates glioblastoma cancer stem-like cell resistance to EGFR-targeted inhibition. *Neoplasia* **14**, 420-428 (2012).
12. F. Snyder, M. L. Blank, H. P. Morris, Occurrence and nature of O-alkyl and O-alk-I-enyl moieties of glycerol in lipids of Morris transplanted hepatomas and normal rat liver. *Biochim Biophys Acta* **176**, 502-510 (1969).
13. F. Snyder, R. Wood, Alkyl and alk-1-enyl ethers of glycerol in lipids from normal and neoplastic human tissues. *Cancer Res* **29**, 251-257 (1969).
14. J. F. Soodsma, C. Piantadosi, F. Snyder, The biocleavage of alkyl glyceryl ethers in Morris hepatomas and other transplantable neoplasms. *Cancer Res* **30**, 309-311 (1970).
15. M. A. Rampy, A. N. Pinchuk, J. P. Weichert, R. W. Skinner, S. J. Fisher, R. L. Wahl, M. D. Gross, R. E. Counsell, Synthesis and biological evaluation of radioiodinated phospholipid ether stereoisomers. *J Med Chem* **38**, 3156-3162 (1995).
16. K. L. Meyer, S. W. Schwendner, R. E. Counsell, Potential tumor or organ-imaging agents. 30. Radioiodinated phospholipid ethers. *J Med Chem* **32**, 2142-2147 (1989).
17. M. A. Rampy, R. S. Brown, A. N. Pinchuk, J. P. Weichert, R. W. Skinner, S. J. Fisher, R. L. Wahl, M. D. Gross, S. P. Ethier, R. E. Counsell, Biological disposition and imaging of a radioiodinated alkylphosphocholine in two rodent models of breast cancer. *J Nucl Med* **37**, 1540-1545 (1996).
18. A. N. Pinchuk, M. A. Rampy, M. A. Longino, R. W. Skinner, M. D. Gross, J. P. Weichert, R. E. Counsell, Synthesis and structure-activity relationship effects on the tumor avidity of radioiodinated phospholipid ether analogues. *J Med Chem* **49**, 2155-2165 (2006).
19. L. Kuerschner, D. Richter, H. K. Hannibal-Bach, A. Gaebler, A. Shevchenko, C. S. Ejsing, C. Thiele, Exogenous ether lipids predominantly target mitochondria. *PLoS One* **7**, e31342 (2012).
20. W. J. van Blitterswijk, M. Verheij, Anticancer mechanisms and clinical application of alkylphospholipids. *Biochim Biophys Acta* **1831**, 663-674 (2013).
21. A. H. van der Luit, S. R. Vink, J. B. Klarenbeek, D. Perrissoud, E. Solary, M. Verheij, W. J. van Blitterswijk, A new class of anticancer alkylphospholipids uses lipid rafts as membrane gateways to induce apoptosis in lymphoma cells. *Mol Cancer Ther* **6**, 2337-2345 (2007).
22. D. Lingwood, K. Simons, Lipid rafts as a membrane-organizing principle. *Science* **327**, 46-50 (2010).
23. Y. C. Li, M. J. Park, S. K. Ye, C. W. Kim, Y. N. Kim, Elevated levels of cholesterol-rich lipid rafts in cancer cells are correlated with apoptosis sensitivity induced by cholesterol-depleting agents. *Am J Pathol* **168**, 1107-1118 (2006).
24. M. Zorniak, P. A. Clark, H. E. Leeper, M. D. Tipping, D. M. Francis, K. R. Kozak, M. S. Salamat, J. S. Kuo, Differential expression of 2',3'-cyclic-nucleotide 3'-phosphodiesterase and neural lineage markers correlate with glioblastoma xenograft infiltration and patient survival. *Clin Cancer Res **18***, 3628-3636 (2012).

25. L. Qiang, Y. Yang, Y. J. Ma, F. H. Chen, L. B. Zhang, W. Liu, Q. Qi, N. Lu, L. Tao, X. T. Wang, Q. D. You, Q. L. Guo, Isolation and characterization of cancer stem like cells in human glioblastoma cell lines. *Cancer Lett* **279**, 13-21 (2009).
26. S. Peickert, J. Waurig, C. Dittfeld, A. Dietrich, Y. Garbe, L. Kabus, M. Baumann, M. Grade, T. Ried, L. A. Kunz-Schughart, Rapid re-expression of CD133 protein in colorectal cancer cell lines in vitro and in vivo. *Lab Invest* **92**, 1607-1622 (2012).
27. A. Hackshaw, C. Harmer, U. Mallick, M. Haq, J. A. Franklyn, 131I activity for remnant ablation in patients with differentiated thyroid cancer: A systematic review. *J Clin Endocrinol Metab* **92**, 28-38 (2007).
28. B. Pohlman, J. Sweetenham, R. M. Macklis, Review of clinical radioimmunotherapy. *Expert Rev Anticancer Ther* **6**, 445-461 (2006).
29. R. M. Macklis, B. Pohlman, Radioimmunotherapy for non-Hodgkin's lymphoma: a review for radiation oncologists. *Int J Radiat Oncol Biol Phys* **66**, 833-841 (2006).
30. K. Simons, J. L. Sampaio, Membrane organization and lipid rafts. *Cold Spring Harb Perspect Biol* **3**, a004697 (2011).
31. A. Kusumi, T. K. Fujiwara, N. Morone, K. J. Yoshida, R. Chadda, M. Xie, R. S. Kasai, K. G. Suzuki, Membrane mechanisms for signal transduction: the coupling of the meso-scale raft domains to membrane-skeleton-induced compartments and dynamic protein complexes. *Semin Cell Dev Biol* **23**, 126-144 (2012).
32. S. Staubach, F. G. Hanisch, Lipid rafts: signaling and sorting platforms of cells and their roles in cancer. *Expert Rev Proteomics* **8**, 263-277 (2011).
33. B. Giebel, D. Corbeil, J. Beckmann, J. Hohn, D. Freund, K. Giesen, J. Fischer, G. Kogler, P. Wernet, Segregation of lipid raft markers including CD133 in polarized human hematopoietic stem and progenitor cells. *Blood* **104**, 2332-2338 (2004).
34. H. Wolburg, S. Noell, P. Fallier-Becker, A. F. Mack, K. Wolburg-Buchholz, The disturbed blood-brain barrier in human glioblastoma. *Mol Aspects Med* **33**, 579-589 (2012).
35. T. J. Mangner, J. L. Wu, D. M. Wieland, Solid-Phase Exchange Radioiodination of Aryl Iodides - Facilitation by Ammonium-Sulfate. *Journal of Organic Chemistry* **47**, 1484-1488 (1982).
36. C. N. Svendsen, M. G. ter Borg, R. J. Armstrong, A. E. Rosser, S. Chandran, T. Ostenfeld, M. A. Caldwell, A new method for the rapid and long term growth of human neural precursor cells. *J Neurosci Methods* **85**, 141-152 (1998).
37. M. M. Tomayko, C. P. Reynolds, Determination of subcutaneous tumor size in athymic (nude) mice. *Cancer Chemother Pharmacol* **24**, 148-154 (1989).
38. L. S. Liebeskind, J. Srogl, Heteroaromatic thioether-boronic acid cross-coupling under neutral reaction conditions. *Organic Letters* **4**, 979-981 (2002).
39. E. Pena-Cabrera, A. Aguilar-Aguilar, M. Gonzalez-Dominguez, E. Lager, R. Zamudio-Vazquez, J. Godoy-Vargas, F. Villanueva-Garcia, Simple, general, and efficient synthesis of meso-substituted borondipyrromethenes from a single platform. *Organic Letters* **9**, 3985-3988 (2007).
40. T. V. Goud, A. Tutar, J. F. Biellmann, Synthesis of 8-heteroatom-substituted 4,4-difluoro-4-bora-3a, 4a-diaza-s-indacene dyes (BODIPY). *Tetrahedron* **62**, 5084-5091 (2006).
41. K. Kemper, M. R. Sprick, M. de Bree, A. Scopelliti, L. Vermeulen, M. Hoek, J. Zeilstra, S. T. Pals, H. Mehmet, G. Stassi, J. P. Medema, The AC133 epitope, but not the CD133 protein, is lost upon cancer stem cell differentiation. *Cancer Res* **70**, 719-729 (2010).

Acknowledgments: L. Rodenkirch was helpful in obtaining the confocal microscopy images and A. Nomura assisted with animal model maintenance. We appreciate advice and the Pirc rat model from W. Dove. **Funding:** Clinical brain tumor imaging was supported by NCI (RO1-158800) and an UW Institute for Clinical and Translational Research pilot grant (9U54TR000021). Clinical lung cancer imaging and iodine-131 therapy trials were funded by Cellectar Biosciences, Inc. J.M.F. was partially supported by NIH training grants (Radiological Sciences T32CA009206, UW MSTP T32GM008692). General funding provided by UW Carbone Cancer Center, Wisconsin Partnership Program core grant support of the Center for Stem Cell and Regenerative Medicine, from the University of Wisconsin (Graduate School and Dept. of Neurological Surgery), and support for J.S.K. from the HEADRUSH Brain Tumor Research Professorship and Roger Loff Memorial Fund for GBM Research. Pilot grants and small animal imaging were supported by the UW Carbone Cancer Center National Cancer Institute Support grant (P30 CA014520) and the University of Wisconsin (Graduate School, Depts. of Radiology, Medical Physics, Human Oncology, Neurological Surgery, Wisconsin Alumni Research Foundation, and Wisconsin Institutes of Discovery). **Author contributions:** A.V. designed and carried out the biological assays. I.K.K. designed and conducted the biological assays and confocal microscopic imaging. P.A.C. designed and conducted all biological assays related to cancer stem cells, interpreted data, and co-wrote and edited the manuscript. K.S. and H.C. conducted experiments with cancer stem cells and xenografts. W.C. helped design biological assays. M.L. formulated all agents for in vivo injection. A.P. synthesized and analyzed all APC analogs. J.G. and M.F. performed preclinical in vivo PET/CT imaging and quantification studies. J.G. and B.T. performed clinical image analysis and quantification. P.P. analyzed clinical images and helped edit the manuscript. J.F. carried out preclinical PET image acquisition, reconstruction, and quantification. A.T. and L.H. recruited patients for imaging studies and interpreted all clinical PET/CT images. C.P. interpreted data, co-wrote and edited the manuscript. J.S.K. recruited patients for imaging studies, designed experiments, interpreted data, provided administrative support, co-wrote and edited the manuscript. J.P.W. carried out radioiodination procedures, designed experiments, interpreted preclinical data, provided administrative support, co-wrote and edited the manuscript. **Competing interests:** J.P.W. and M.A.L. are cofounders of Cellectar Biosciences, Inc., which owns licensing and patent rights to CLR1404 and related compounds described in this paper. P.J.P. and authors associated with Cellectar Biosciences, Inc. were employees of and/or shareholders in Cellectar Biosciences, Inc. All other authors declare that they have no competing interests. **Data and materials availability:** CLR analogs and GSC lines can be requested via material transfer agreements from Cellectar Biosciences or University of Wisconsin-Madison, respectively.

Figure captions

Figure 1. Alkylphosphocholine (APC) analog chemical structures. CLR1404 could be synthesized as a radioactive compound (^{125}I-, ^{124}I-, or ^{131}I-); as a fluorescent analog, CLR1501; or as a near-IR analog, CLR1502.

Figure 2. Uptake of CLR1404 analogs in human cancer cell lines. (**A**) Fluorescence confocal microscopy shows CLR1501 (5 μM) uptake in multiple cancer types, and less uptake in normal human fibroblasts at 24 hours. Scale bar, 10 μm. (**B**) Co-culture of human prostate cancer (PC-3) cells and normal human fibroblasts. Cells were treated with the fluorescent analog CLR1501 (5 μM) for 24 h and counter-stained with the nuclear stain, Hoechst 33342. Scale bar, 10 μm. (**C**) Quantitative uptake and retention of ^{125}I-CLR1404 in three cancer cell lines derived from patients and the corresponding patient-matched normal cell lines. Data are means ± S.E.M. (*n* = 3 independent experiments with 3 biological replicates each). *P<0.001, ANOVA with post-hoc Tukey test.

Figure 3: **CLR1501 fluorescent labeling of GSCs in vitro.** (**A**) Glioblastoma stem-like cells (GSCs, line 99) were treated overnight with CLR1501. CLR1501 uptake was visualized with confocal microscopy and compared to matched serum-cultured GBM cells (serGBM), normal human astrocytes, and human neural stem cells (NSC). (**B**) Flow cytometry was performed to quantify CLR1501 uptake after 24 hours in GSC patient-specific lines 12.1, 22, 33, 44, 99; serGBM lines 22, 33, 99, U251, U87; NSCs; and astrocytes. Data are means ± SD of 3 independent experiments. *P<0.05, Student's t-test compared to astrocyte. (**C**) CLR1501 labeling of the $CD133^+$ sub-population of GSCs was analyzed using flow cytometry. Data are means ± SD of 3 independent experiments. *P<0.05 versus line-matched $CD133^+$ or $CD133^-$ cells; #P<0.05 versus NSCs; Student's t-test.

Figure 4. ^{124}I-CLR1404 uptake in a broad range of tumors. Images shown are microPET or PET/CT, or fused brain MRI/PET. Yellow arrows show xenografts; green arrow points to liver metastasis. **(A)** Xenografts of human cancer cell lines: brain (U87 in nude rat), colon (HCT-116, HT-29), triple-negative breast (MDA-MB-231), prostate (PC3), pancreatic (BxPC3), and Ewing's sarcoma. **(B)** Rodent tumor models: bladder (mouse SV40), breast (mouse 4T1), pancreatic (c-myc transgenic mouse), brain (rat CNS-1).

Figure 5: **CLR1501 labeling of GSCs in vivo.** CLR1501 was administered to mice harboring GSC-derived orthotopic gliomas 4 days prior to sacrifice. (**A** and **B**) Confocal microscopy verified CLR1501 uptake in histologically confirmed tumor (A: CLR1501=green; B: H&E, T=tumor). (**C** to **E**) Immunohistochemistry for stem cell markers, including human-specific nestin (C), Olig2 (D), and CD15/SSEA-1 (E). DAPI (blue) is shown in merged images. (**F** and **G)** Ex vivo flow cytometry analysis with

CD133 (105 GSC-derived tumor-1) to quantify $CD133^{+}/CLR1501^{+}$ co-localization in GSC-derived and U251 xenografts. The % of marker-positive cells in total number of tested tumor cells is listed in **G**.

Figure 6. **Tumor growth and animal survival after ^{131}I-CLR1404 therapy.** Nude mice harboring human tumor xenografts (*n*= 6 renal, 6 colorectal, 5 ovarian, and 9 breast) were administered a single ^{131}I-CLR1404 dose (arrow). Control animals were administered a mass-equivalent CLR1404 dose (*n*=6). Data are mean tumor volumes +/- SEM. *P*-values for tumor growth curves determined by one way repeated measurement ANOVA. *P*-values for survival curves were constructed by Kaplan-Meier method and analyzed via Log-rank test .

Figure 7. Imaging of brain tumor patients and patient-derived xenografts. (**A**) Metastatic NSCLC patient: PET imaging six days after i.v. ^{124}I-CLR1404 administration revealed three previously unknown brain lesions suspicious for metastases (3D reconstruction). Lesions were verified via contrast-enhanced MRI (T1-Gd, arrow), but not detected on surveillance ^{18}F-FDG PET/CT, and present on ^{124}I-CLR1404 PET (dotted line=axial PET section). (**B** to **D**) Patient diagnosed with suspected left insular GBM on T1-gadolinium-enhanced (B) and T2-weighted (C) MRI, was confirmed on surgical pathology. Preoperative PET imaging obtained two days after i.v. ^{124}I-CLR1404 administration revealed heterogeneous tumor uptake in a different pattern than T1-contrasted MRI, with low background signal in venous sinus blood pool (arrows) and normal brain (tumor/brain ratio = 28) (D). (**E** to **I**) Fluorescent CLR1502 imaging 4 days after administration showed uptake and localization in line 107 GSC-derived xenografts (E). Histological confirmation of line 107 GSC-derived xenografts: H&E (F and G) and human-specific nestin staining (brown in H and I).

Figure 1

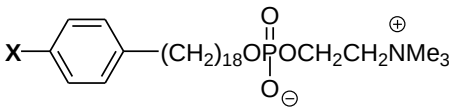

^{131}I-CLR1404	X = ^{131}I	Radioisostere; molecular radiotherapeutic
^{124}I-CLR1404	X = ^{124}I	Radioisostere; PET imaging
^{125}I-CLR1404	X = ^{125}I	Radioisostere
CLR1401	X = ^{127}I	Non-radioactive isostere; chemotherapeutic

CLR1501 X = 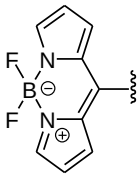 Fluorescent analog

CLR1502 X = 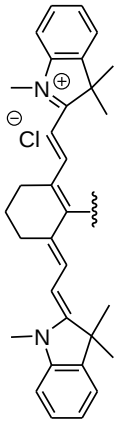 Near-infrared analog

Figure 2.

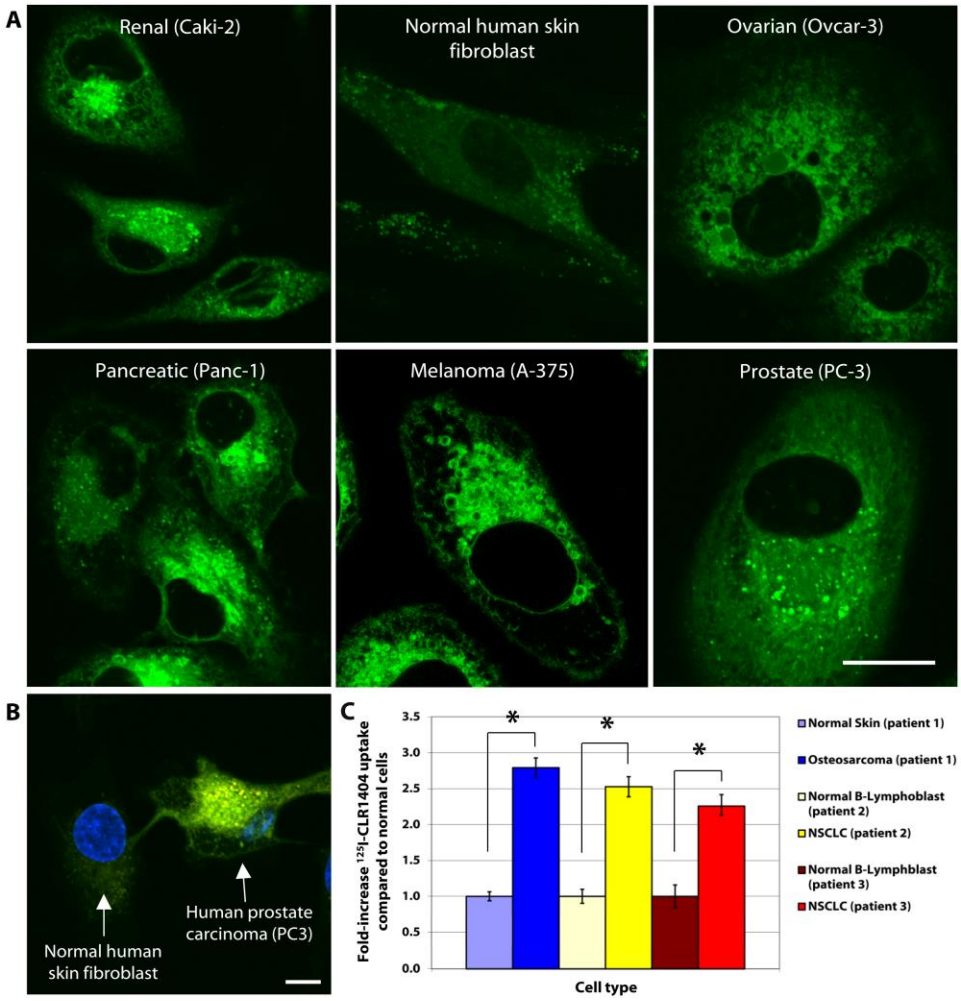
A
Renal (Caki-2)
Normal human skin fibroblast
Ovarian (Ovcar-3)
Pancreatic (Panc-1)
Melanoma (A-375)
Prostate (PC-3)
B
Human prostate carcinoma (PC3)
Normal human skin fibroblast
C
Fold-increase 125I-CLR1404 uptake compared to normal cells
3.5
3.0
2.5
2.0
1.5
1.0
0.5
0.0
Cell type
Normal Skin (patient 1)
Osteosarcoma (patient 1)
Normal B-Lymphoblast (patient 2)
NSCLC (patient 2)
Normal B-Lymphblast (patient 3)
NSCLC (patient 3)

Figure 3.

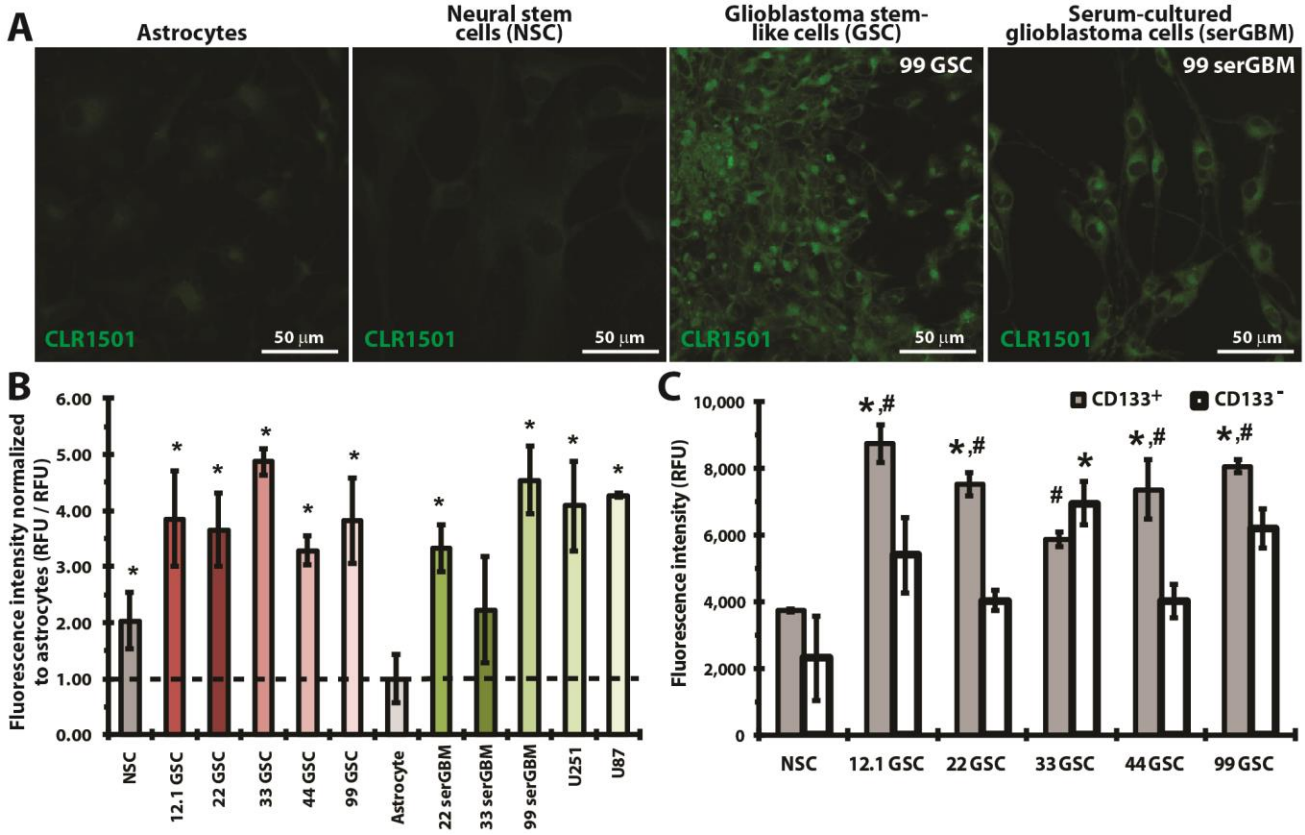
A
Astrocytes
Neural stem cells (NSC)
Glioblastoma stem-like cells (GSC)
Serum-cultured glioblastoma cells (serGBM)
99 GSC
99 serGBM
CLR1501
50 μm
B
Fluorescence intensity normalized to astrocytes (RFU / RFU)
NSC
12.1 GSC
22 GSC
33 GSC
44 GSC
99 GSC
Astrocyte
22 serGBM
33 serGBM
99 serGBM
U251
U87
C
Fluorescence intensity (RFU)
CD133+
CD133-
NSC
12.1 GSC
22 GSC
33 GSC
44 GSC
99 GSC

Figure 4.

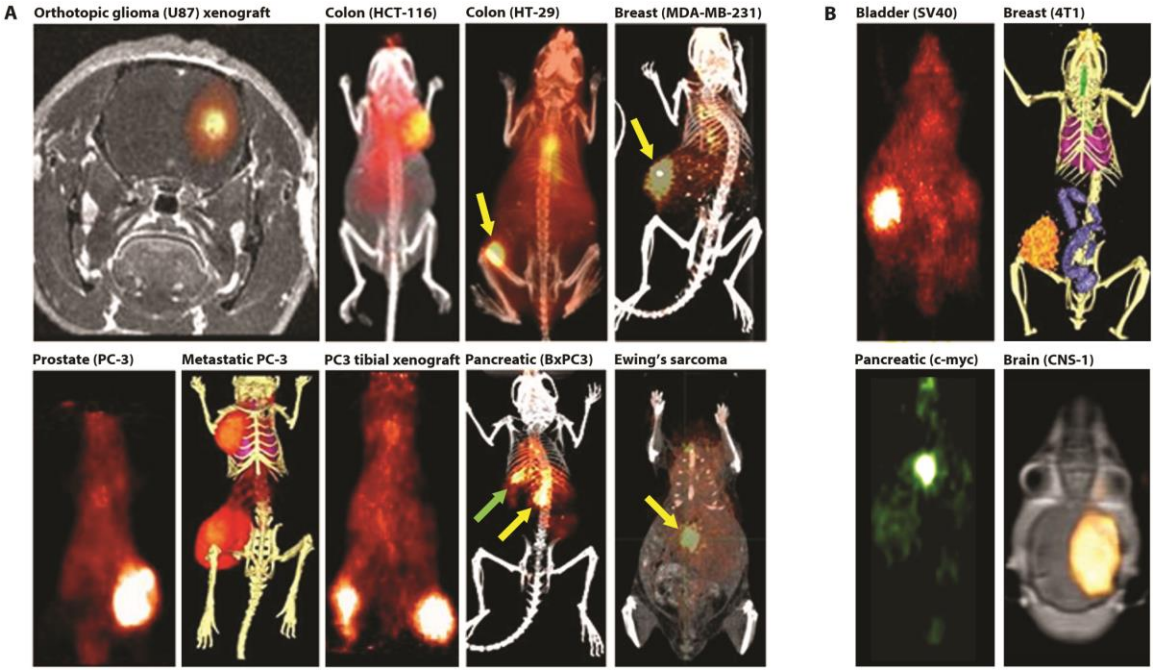
A
Orthotopic glioma (U87) xenograft
Colon (HCT-116)
Colon (HT-29)
Breast (MDA-MB-231)
Prostate (PC-3)
Metastatic PC-3
PC3 tibial xenograft
Pancreatic (BxPC3)
Ewing's sarcoma
B
Bladder (SV40)
Breast (4T1)
Pancreatic (c-myc)
Brain (CNS-1)

Figure 5.

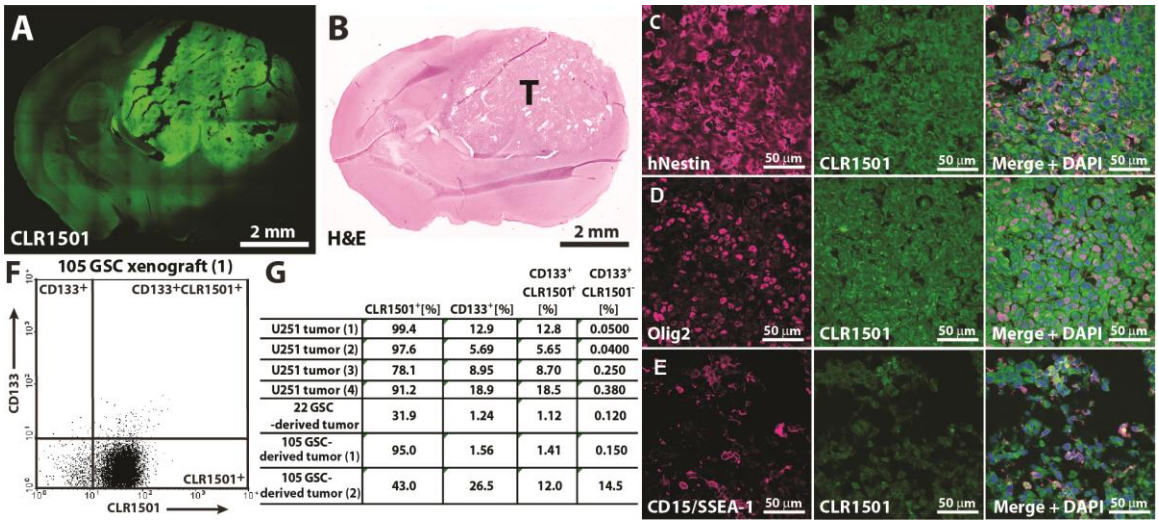

G

	CLR1501$^+$[%]	CD133$^+$[%]	CD133$^+$ CLR1501$^+$ [%]	CD133$^+$ CLR1501$^-$ [%]
U251 tumor (1)	99.4	12.9	12.8	0.0500
U251 tumor (2)	97.6	5.69	5.65	0.0400
U251 tumor (3)	78.1	8.95	8.70	0.250
U251 tumor (4)	91.2	18.9	18.5	0.380
22 GSC -derived tumor	31.9	1.24	1.12	0.120
105 GSC-derived tumor (1)	95.0	1.56	1.41	0.150
105 GSC-derived tumor (2)	43.0	26.5	12.0	14.5

Figure 6.

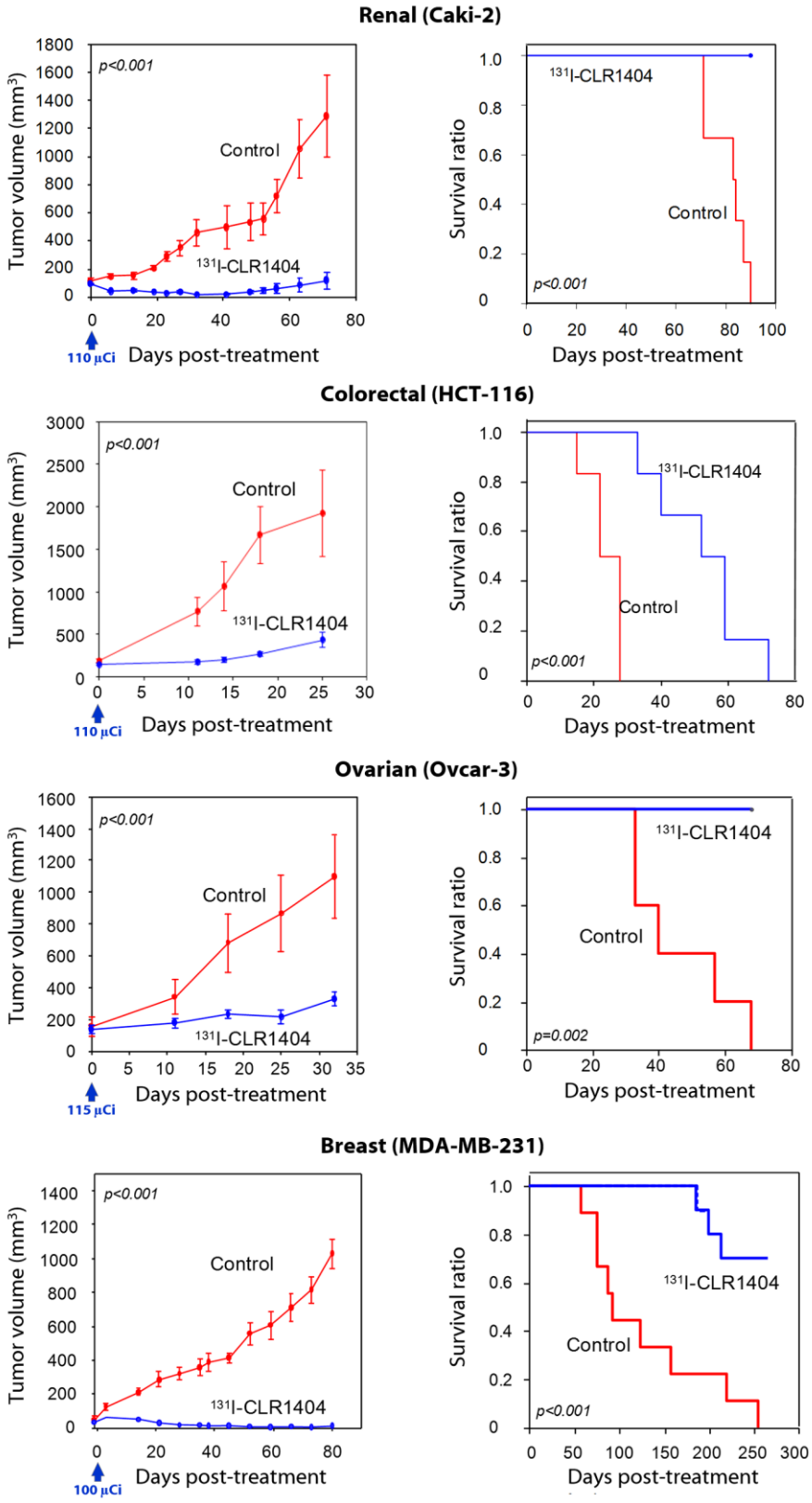
Renal (Caki-2)
Tumor volume (mm³)
p<0.001
Control
131I-CLR1404
110 µCi
Days post-treatment
Survival ratio
131I-CLR1404
Control
p<0.001
Days post-treatment
Colorectal (HCT-116)
Tumor volume (mm³)
p<0.001
Control
131I-CLR1404
110 µCi
Days post-treatment
Survival ratio
131I-CLR1404
Control
p<0.001
Days post-treatment
Ovarian (Ovcar-3)
Tumor volume (mm³)
p<0.001
Control
131I-CLR1404
115 µCi
Days post-treatment
Survival ratio
131I-CLR1404
Control
p=0.002
Days post-treatment
Breast (MDA-MB-231)
Tumor volume (mm³)
p<0.001
Control
131I-CLR1404
100 µCi
Days post-treatment
Survival ratio
131I-CLR1404
Control
p<0.001
Days post-treatment

Figure 7.

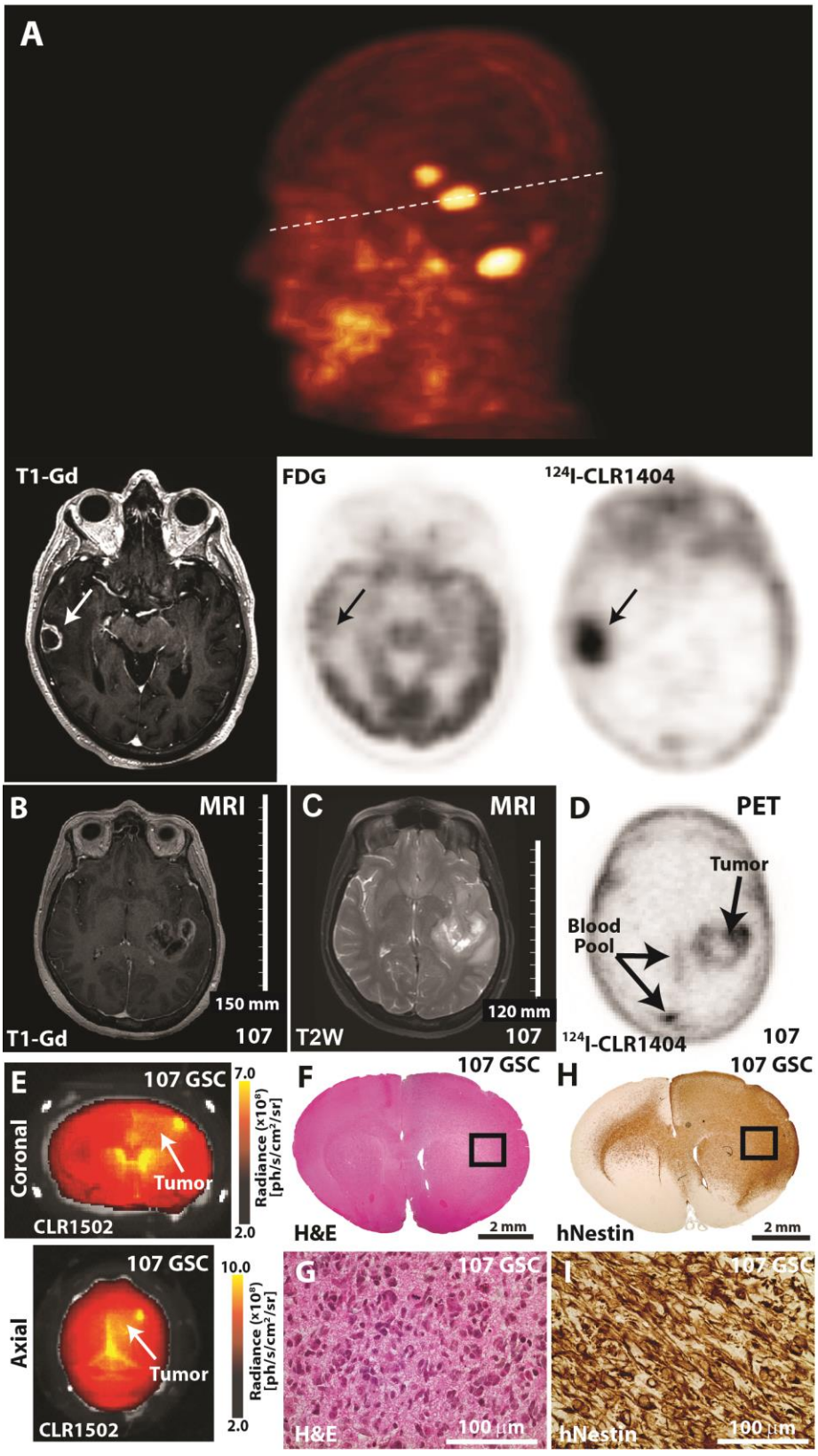
A
T1-Gd
FDG
124I-CLR1404
B
MRI
150 mm
T1-Gd
107
C
MRI
120 mm
T2W
107
D
PET
Tumor
Blood Pool
124I-CLR1404
107
E
107 GSC
Coronal
Tumor
CLR1502
7.0
2.0
Radiance (x10^6) [ph/s/cm²/sr]
F
107 GSC
H&E
2 mm
H
107 GSC
hNestin
2 mm
Axial
107 GSC
Tumor
CLR1502
10.0
2.0
Radiance (x10^6) [ph/s/cm²/sr]
G
107 GSC
H&E
100 μm
I
107 GSC
hNestin
100 μm

SUPPLEMENTARY MATERIALS

Supplementary Methods

Synthesis of CLR1501

The synthesis of CLR1501 (18-[p-(4,4-difluoro-4-bora-3a,4a-diaza-s-indacene-8-yl)-phenyl]-octadecyl phosphocholine) (fig. S10A) was performed using Liebeskind-Srogl cross-coupling reaction (38) of 18-[*p*-(dihydroxyboryl)-phenyl]-octadecyl phosphocholine [**2**] with 8-thiomethyl-BODIPY [**1**] according to the published procedure (39). 8-(Thiomethyl-4,4-difluoro-4-bora-3a,4a-diaza-*s*-indacene [**1**] as well as compound [**2**] were synthesized as previously described (40).

^{1}H NMR (500 MHz, $CDCl_3$ - CD_3OD 1:1): δ 7.93 (s, 2H), 7.52 (dt, J_1 = 8.3 Hz, J_2 = 1.8 Hz, 2H), 7.38 (dt, J_1 = 8.3 Hz, J_2 = 1.8 Hz, 2H), 7.02 (d, J = 4.1 Hz, 2H), 6.595 (dd, J_1 = 4.1 Hz, J_2 = 1.7 Hz, 2H), 4.23 (br m, 2H), 3.87 (q, J = 6.6 Hz, 2H), 3.60 (m, 2H), 3.22 (s, 9H), 2.75 (t, J = 7.6 Hz, 2H), 1.71 (quintet, J = 7.4 Hz, 2H), 1.64 (quintet, J = 7.1 Hz, 2H), 1.44 – 1.24 (m, 28H). ^{19}F NMR (376.2 MHz, $CDCl_3$ - CD_3OD 1:1): δ -145.8 (q, J = 28 Hz). ESI ultra high-res QTOF MS (*m/z*) calculated for $C_{38}H_{60}BF_2N_3O_4P$ ($[M+H]^+$) 701.441339, found 701.44041; calculated for $C_{38}H_{59}BF_2N_3O_4PNa$ ($[M+Na]^+$) 723.423283, found 723.42221.

Synthesis of CLR1502

CLR1502 was synthesized (fig. S10B) by the Suzuki cross-coupling reaction of 18-[p-(dihydroxyboryl)-phenyl]-octadecyl phosphocholine [**2**] with commercially available fluorescent dye IR-775 in the presence of a catalyst, Pd-PEPPSI-IPr. CLR1403 (1.322 g, 2.38 mmol), dye IR-775 chloride (1.856 g, 3.57 mmol), potassium carbonate (987 mg, 7.14 mmol) and Pd-PEPPSI-IPr (80 mg, 0.12 mmol) were placed in a 100 ml round-bottom flask and kept under high vacuum for 30 min. Degassed methanol was added via cannula and the reaction mixture was stirred at room temperature for 20 h checked by TLC in 3 systems: silica gel ($CHCl_3$-MeOH-H_2O 10:6.5:1.5) and $CHCl_3$-MeOH-conc NH_4OH 65:25:4) and also amino-silica gel ($CHCl_3$-MeOH-H_2O 65:25:1). Chloroform (10-15 ml) was added and the mixture was filtered using a glass fritted funnel to remove inorganic salts. Filtrate was loaded on silica gel column. The column was eluted first with stepwise gradient of $CHCl_3$ - MeOH (90:10, 80:20, 50:50) - 500 ml each and finally with $CHCl_3$ – MeOH – H_2O (65:25:4) – 1880 ml, then with $CHCl_3$ – MeOH – H_2O (65:35:5) – 380 ml and finally with $CHCl_3$-MeOH-conc NH_4OH (65:25:4). Fractions containing CLR1502 were combined and analyzed by TLC and NMR. The most pure fraction weighed 889 mg (38%).

^{1}H NMR (500 MHz, $CDCl_3$ - CD_3OD 1:1): δ 7.43 (dm, J = 8 Hz, 2H), 7.37 (dt, J1 = 7.9 Hz, J2 = 1.3 Hz, 2H), 7.31 (d, J = 14.1 Hz), 7.25 (dd, J1 = 7.5 Hz, J2 = 0.9 Hz, 2H), 7.19 (dt, J1 = 7.3 Hz, J2 = 0.9 Hz, 2H), 7.16-7.14 (m, 4H), 6.06 (d, J = 13.9 Hz, 2H), 4.25 (m, 2H), 3.86 (q, J = 6.6, 2H), 3.62 (m, 2H), 3.56 (s, 6H), 3.24 (s, 9H), 2.82 (t, J = 7.3 Hz, 2H), 2.71 (t, J = 6.2 Hz, 2H), 2.08 (m, 2H), 1.76 (m, 2H), 1.62 (quintet, = 7.1 Hz, 2H), 1.48 – 1.24 (m, 28H), 1.21 (s, 12H). ^{31}P NMR (202.3 MHz, $CDCl_3$ - CD_3OD 1:1): 1.07 (s).

ESI ultra high-res QTOF MS (m/z) calcd for $C_{61}H_{89}N_3O_4P$ ([M-Cl]+) 958.65852, found 958.65399; 479.32869 ([M-Cl + H]2+/2).

Normal cell and cancer cell co-culture

The PC-3 (human prostate carcinoma) cell line and normal human fibroblasts were plated overnight on microslide VI (Ibidi). The next day, the cells were treated with 5 µM of CLR1501 for 24 hours. The cells were counter stained with the nuclear stain, Hoechst 33342 (Invitrogen). The cells were examined using Nikon A1R confocal microscope (Keck Laboratory, University of Wisconsin-Madison). The emission signal of CLR1501 was detected using Alexa Fluor 488 filters. Hoechst 33342 was detected using Hoechst filters (ex/em 350/461 nm).

In vitro uptake and retention of ^{125}I-CLR1404

In vitro uptake/retention quantification of ^{125}I-CLR1404 was performed in human cancer and normal cells as follows. Briefly, cells were plated at $5.0x10^4$ cells per well in six well plates using the appropriate serum containing media, and allowed to adhere overnight. The next day, each well was washed with 2 ml of serum-free media after which FBS-containing media with 1.5 µCi of ^{125}I-CLR1404 was added to each well (2 ml media/drug mixture per well, in triplicate). Cells were then incubated at 37^{o}C and 5% CO2 in air for the indicated time period. After various times of incubation, for each replicate, the media was removed and wells were washed twice with 1ml of 1× PBS containing 0.1% BSA. The cells were then trypsinized, scraped, mixed and divided evenly into two 0.5 ml aliquots. For sample measurement, radioactivity in 10 µl from each sample was measured with a gamma counter for ^{125}I using a commercial ^{125}I standard and a standard curve using serial diluted ^{125}I-CLR1404. The other cell fraction aliquot was centrifuged for 30 seconds at 14,000 x g, and the cell pellet was dissolved in 100 µl of 1× PBS. The DNA content was determined by absorbance at 260nm and absorbance at 320 nm was used for turbidity correction. Total cell number was determined by comparison to a standard curve of 260 nm absorbance values of known cell numbers. From this data, radioactivity per cell was calculated as pCi per cell.

Live cell flow cytometry

Cultured human GSCs or other cells were treated for 24 hrs with 10 µM CLR1501 or vehicle (1% ethanol) controls. Approximately 10^6 cells were enzymatically dissociated from spheres and resuspended in flow cytometry buffer (PBS+1% goat serum). Pre-conjugated AC/CD133 with allophycocyanin (APC; Miltenyi Biotech 130-090-826) was added to the suspension (1:11) to label GSCs and incubated for 1 hr on ice. It is important to note that the anti-CD133 antibody used in this study specifically targets the stem cell-specific glycosylated form of AC/CD133, and that other glycosylated or non-glycosylated forms of CD133 protein are likely expressed in the AC/CD133$^-$ population (41). Cells were washed multiple times and analyzed using flow cytometry (FACScalibur, Becton Dickinson). The flow cytometer was corrected for background fluorescence (no antibody control) and spectral bleed-through (compensation with single labeled cells). Data were collected on 10,000 cells by gating for CLR1501 (490/515) and AC/CD133-

APC (650/660), and analyzed using WinMDI freeware (http://facs.scripps.edu/software.html). Live cells were gated using forward (FSC) and side (SSC) scatter. Proper gating was established to quantify positive vs. negative fluorescent cells by comparing to isotype controls. Intensity is represented by relative fluorescent units (RFU) or the geometric mean of resultant histograms (fig. S4). For in vivo studies, tumor xenografts were microscopically dissected from mouse brains with special care to avoid normal brain parenchyma. Tumor pieces were enzymatically dissociated using Accutase for 15 min followed by mechanical trituration with P200 pipette. The resultant slurry was passed through a 40-µm cell strainer before the AC/CD133 staining procedure.

GSC orthotopic xenograft model

All described animal studies were performed according to animal protocols approved by Institutional Animal Care and Use Committee. GSC-derived orthotopic xenografts were initiated as previously described (11,24). Cells were stereotactically injected into the right striatum of anesthetized non-obese diabetic severe combined immunodeficient (NOD-SCID) mice at the following coordinates referenced from bregma: 0 mm antero-posterior, +2.5 mm medio-lateral, and -3.5 mm dorso-ventral. At either 3 months or onset of neurological symptoms, *in vivo* tumor formation was verified using magnetic resonance imaging [mice are anesthetized with isofluorane and contrast enhanced 10 mmol/kg of intra-peritoneal gadodiamide (Omniscan)], placed into a 4.7T horizontal bore small animal MRI scanner (Varian) and T1- and T2-weighted images obtained. After MRI showed tumor xenograft growth or when neurological symptoms were observed, injected NOD-SCID mice were euthanized by perfusion fixation with 4% paraformaldehyde (PFA). Brains were then excised and embedded in paraffin for general histology or processed for frozen sectioning. For CLR1404 studies, after overnight fixation in 4% paraformaldehyde, brains were embedded in OCT compound and frozen for cryostat sectioning at 5-20 µm. This different processing approach was used because CLR1404 and analogs are soluble in the ethanolic dehydration steps required during paraffin processing.

Lipid raft staining and disruption

The cell line, A549 (non-small lung adenocarcinoma) was plated overnight on microslide VI (Ibidi) in serum containing media (F-12 media supplemented with 10% fetal bovine serum). The next day, the cells were incubated with 5 µM CLR1501 at 37ºC for 30 minutes. The cells were then washed with phosphate buffered saline and incubated with Cholera Toxin β-subunit (CTB) and anti-CTB for 10 and 15 minutes, respectively at 4ºC to label ganglioside GM1. The cells were fixed with 4% formaldehyde at 4ºC for 15 minutes and washed with phosphate buffered saline. Cholesterol was stained using 0.5 mg/ml filipin III for 30 minutes at 37ºC.

PC-3 cells were pretreated with either 2 µg/ml Filipin III or vehicle for 15 min, then washed and incubated with 2 µCi of ^{125}I-CLR1404 for 1 hour. The media was removed and the cells were washed with phosphate buffered saline containing 0.1%

bovine serum albumin, trypsinized, then split into two samples for determination of cell number by DNA content (A_{280} compared to a cell line specific standard curve) and counts per minute using a Gamma Counter (Perkin Elmer). It is important to note that higher Filipin III concentrations are cytotoxic, and therefore complete lipid raft ablation (and presumably complete CLR1404 analog uptake inhibition) could not be accomplished.

Immunohistochemistry

Primary and secondary antibodies were purchased commercially: human-specific nestin (MAB5326, Millipore), Olig2 (sc-48817, Santa Cruz Biotechnology), and CD15/SSEA-1 (555400, BD Pharmingen); and goat anti-IgG secondary antibodies Alexa Fluor 488 and 568 (Invitrogen). Frozen GSC xenograft samples were first rehydrated to water. Samples were then blocked in 10% goat serum for 1 hour prior to overnight incubation in primary antibody. After thorough rinsing with PBS, species-specific secondary antibody was applied for 1 h. Last, nuclear counterstaining with DAPI or TO-PRO-3 was performed prior to mounting in aqueous mounting medium (Prolong Gold Antifade reagent, Invitrogen).

MicroPET tumor imaging with ^{124}I-CLR1404 and ^{18}F-FDG in the presence of inflammation

Prostate tumor cells (1×10^6 PC3 cells in 100 µl PBS) were implanted into the thigh muscle on one leg and injected directly into the tibia (via knee joint) of the contralateral leg to simulate a bone metastasis in nude mice (n = 6). A carageenan-induced granuloma (600 µl air pouch injected with 200 µl 1% carageenan in sterile water) was created subcutaneously between the scapulae in each mouse. Five days after induction of the granuloma, ^{18}F-FDG (200 µCi, 0.1 ml) was injected intravenously via lateral tail vein into anesthetized (isoflurane) mice. One hour later, while under anesthesia, animals underwent whole body microPET scanning (Siemens Inveon, 40 million counts collected). Following scanning, animals were injected intravenously with ^{124}I-CLR1404 (0.2 ml, 85-110 µCi), Comparative microPET scans were performed 24 hrs later under identical conditions. By this time the ^{18}F signal had returned to background levels. Granulomas to tumor ratios were calculated by ROI analysis.

SUPPLEMENTARY FIGURES

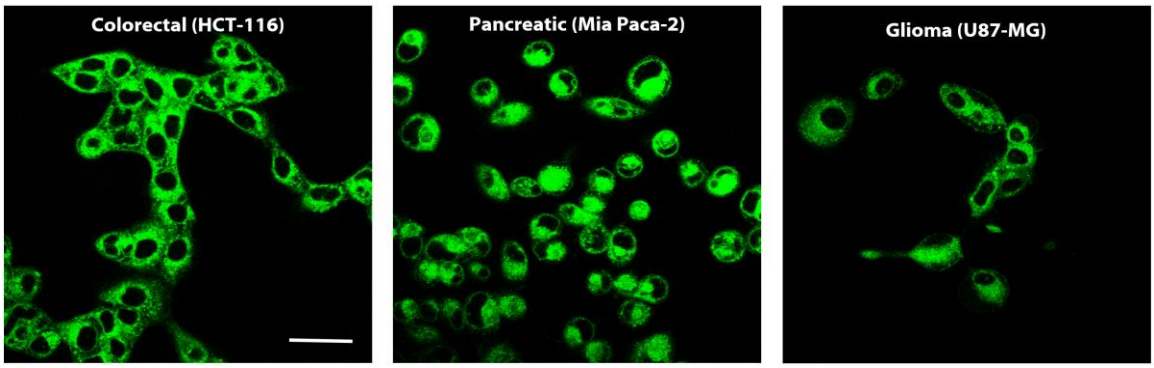

Figure S1. **Preferential cancer cell uptake of CLR1501**. Fluorescence confocal microscopy illustrates that the fluorescent CLR1404 analogue, CLR1501, is selectively retained in three additional cancer types at 24 hours post treatment. The other cell lines are shown in Fig. 2A. Scale bar, 10 µm.

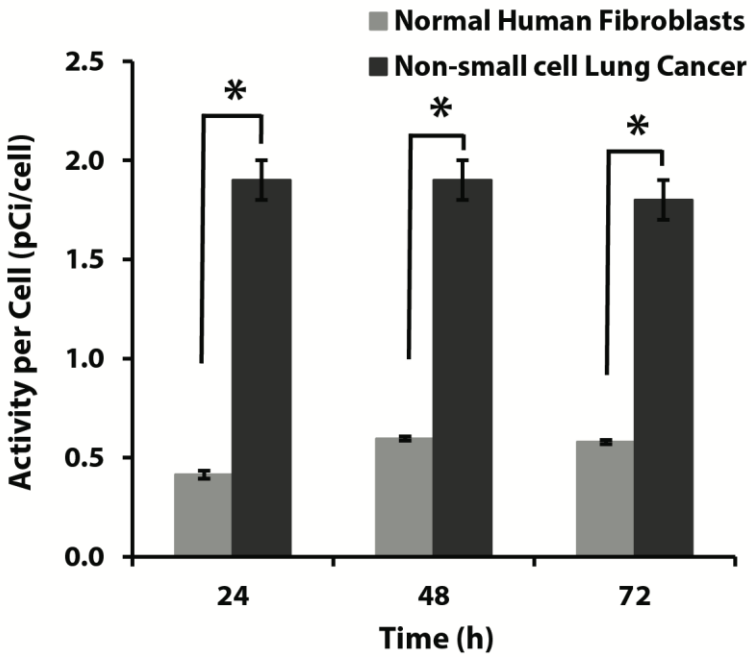

Figure S2. Preferential ^{125}I-CLR1404 uptake and retention in cancer cells in vitro. Uptake and retention of ^{125}I-CLR1404 in the A549 human NSCLC cell line relative to normal primary human fibroblasts at various time points. Data are means ± S.E.M. (*n* = 3 independent experiments with 3 biological replicates each). *P<0.001, ANOVA with post-hoc Tukey test.

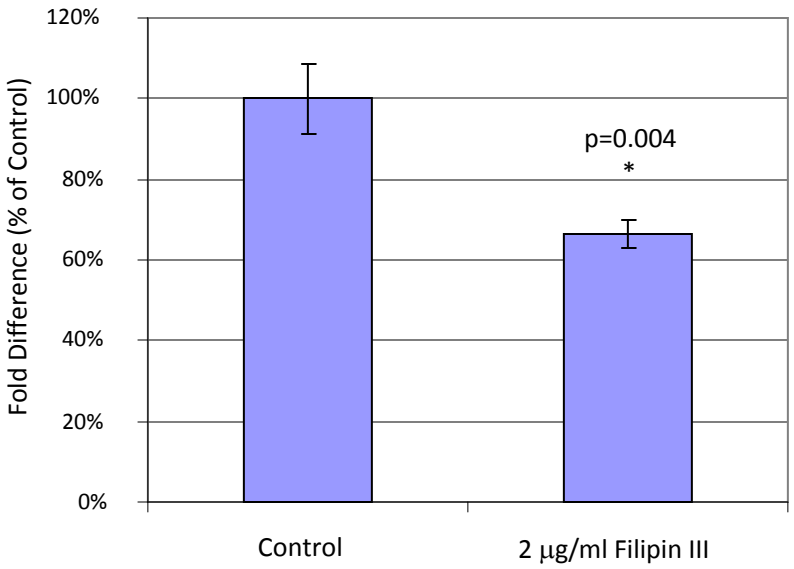

Figure S3. Uptake and retention of ^{125}I-CLR1404 after lipid raft disruption in prostate carcinoma cells. PC-3 cells were pretreated with either Filipin III or vehicle, then incubated with ^{125}I-CLR1404 for 1 h. DNA content (compared to a cell line–specific standard curve) and counts per minute were calculated. Data are average percent of control ± SEM (*n* = 6). *P*-value determined by t-test.

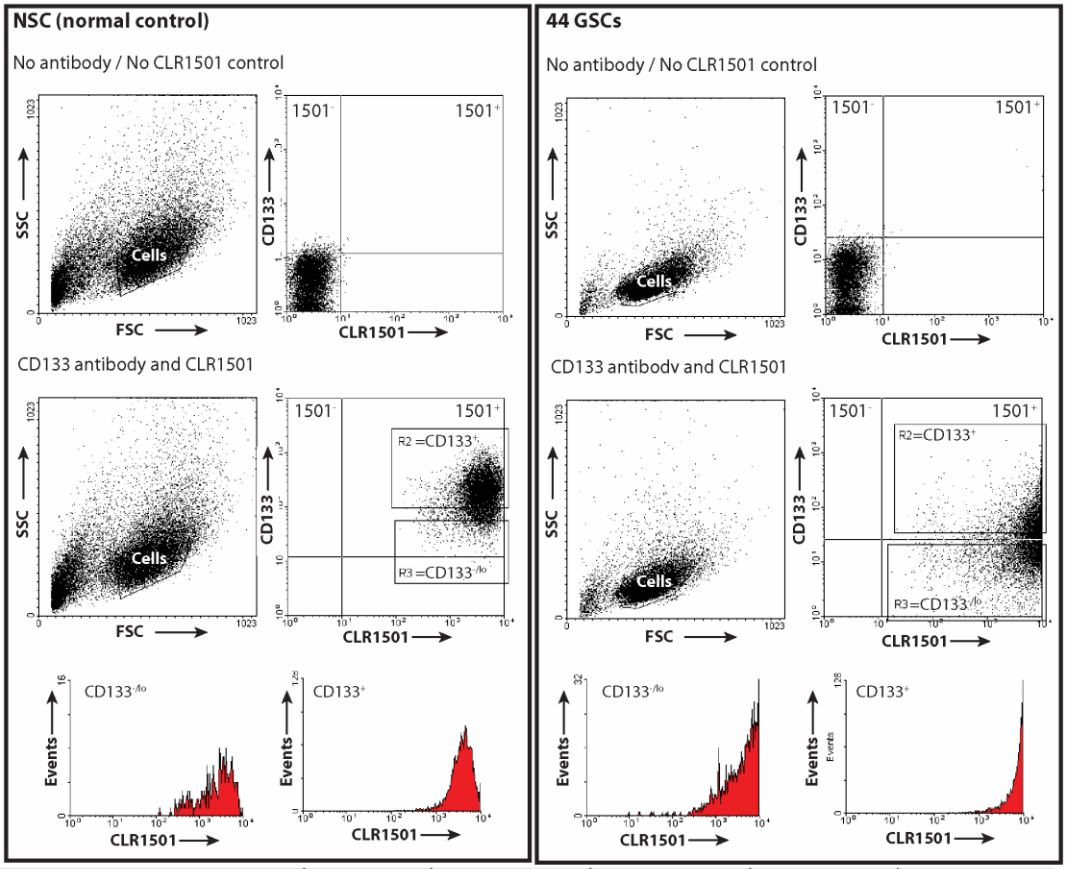

	NSC	12.1 GSC	22 GSC	33 GSC	44 GSC	99 GSC
Gmean [RFU]	3570 ± 169	7380 ± 1010	7410 ± 301	6160 ± 487	5780 ± 756	7860 ± 193
CD133^{+} [RFU]	3740 ± 53.3	8740 ± 560	7530 ± 352	5860 ± 237	7350 ± 895	8050 ± 205
CD133^{-} [RFU]	2290 ± 1250	5380 ± 1130	4030 ± 303	6940 ± 659	4010 ± 486	6190 ± 593
p-value CD133^{+} vs CD133^{-}	0.12	0.02	0.0037	0.047	0.0088	0.016
p-value GSC vs NSC	N/A	0.00046	0.00027	0.00011	0.0022	3.90e-06

Figure S4: **Flow cytometry analysis of CLR1501 GSC labeling.** After overnight labeling with CLR1501, GSC and NSC spheres were dissociated to single cells, immunolabeled with CD133, and analyzed by flow cytometry. Cellular fraction was first gated by SSC/FSC plots. Baseline values were determined through use of no CLR1501 / no primary antibody controls for each cell line, and used to construct quadrants for positive and negative labeling of cells. With the CD133 antibody, regions were chosen to represent CD133^{+} and CD133$^{-/lo}$ populations of GSCs and NSCs. These regions were analyzed for average fluorescent intensity (geometric mean), which is presented in the table from triplicate flow cytometry runs. Data in table are means ± SD of 3 independent experiments. *P*-values determined by Student's t-test.

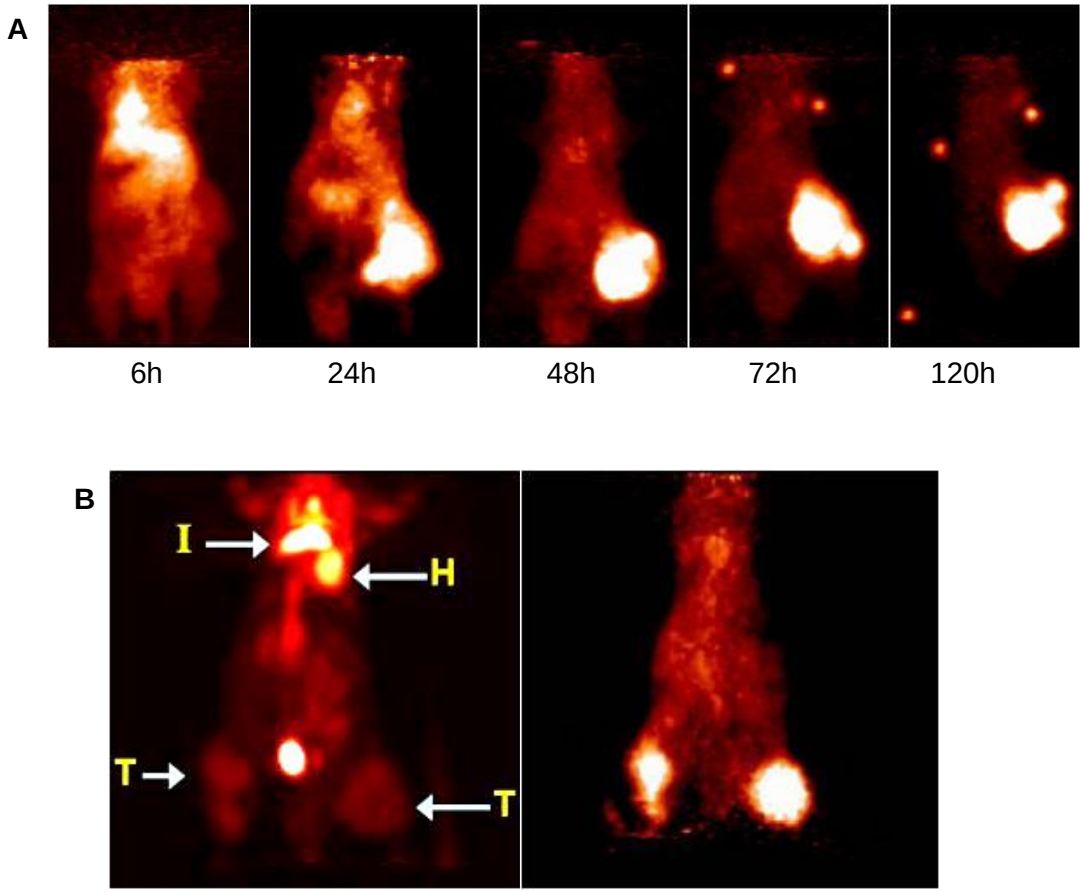

Figure S5. **In vivo time course of biodistribution and tumor uptake of ^{124}I-CLR1404 and ^{18}F-FDG in a prostate tumor model.** (**A**) A SCID mouse bearing a subcutaneous flank PC-3 (human prostate carcinoma) xenograft. Spatial fiducial markers in the 72 h and 120 h panels were used for image fusion. (**B**) MicroPET projection view images of a mouse with human PC3 tumors (T) in the right flank and pseudo metastasis in the left tibia (T), a Carageenan-induced inflammatory lesion (I) located between the scapulae, and heart (H). Left image was acquired 1 h after administration of ^{18}F-FDG. Right image was obtained 24 h after administering ^{124}I-CLR1404 to the same mouse 24 h after the FDG scan.

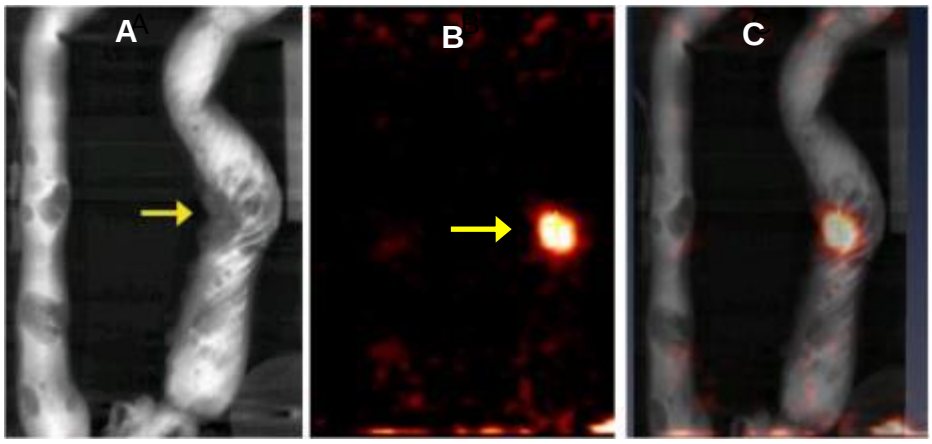

Figure S6. Dual modality PET/CT virtual colonoscopy. (**A** to **C**) An excised PIRC rat colon filled with 2% barium positive contrast and imaged with 2D-microCT projection (A) and ^{124}I-NM404 microPET (B). The fusion of (A and B) is shown in (C). The only tumor (arrow) that was positive on ^{124}I-CLR404 microPET was the only malignant one of 20 total colon lesions (movie S2).

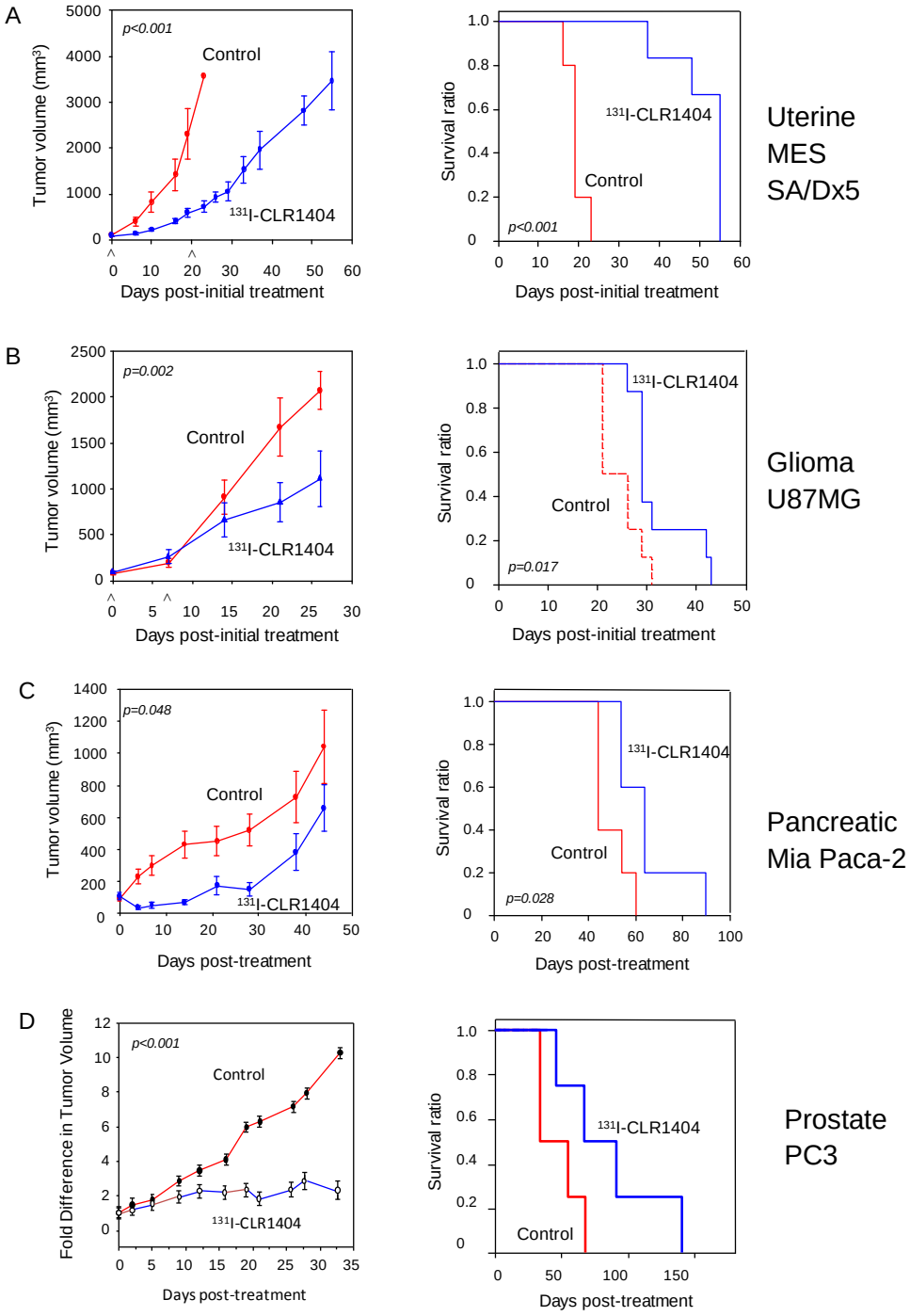

Figure S7. **Tumor growth and animal survival after ^{131}I-CLR1404 therapy.** Radiotherapy in human tumor xenografts was tested. ^{131}I-CLR1404 dosing was as follows: (**A**) uterine, day 0 130 µCi, day 20 145 µCi (*n* = 6); (**B**) glioma, days 0 and 7, 100 µCi each (*n* = 8); (**C**) pancreatic, day 0 125 µCi (*n* = 5); (**D**) prostate, day 7, 100 µCi (*n* = 6). Control animals (*n* = 6) were administered an approximate mass-equivalent of non-radioactive CLR1404 dose on Day 0. Tumor volumes are means ± SEM. Survival curves were constructed by Kaplan-Meier method and analyzed via Log-rank test for significance. *P*-values determined by one-way repeated measurement ANOVA.

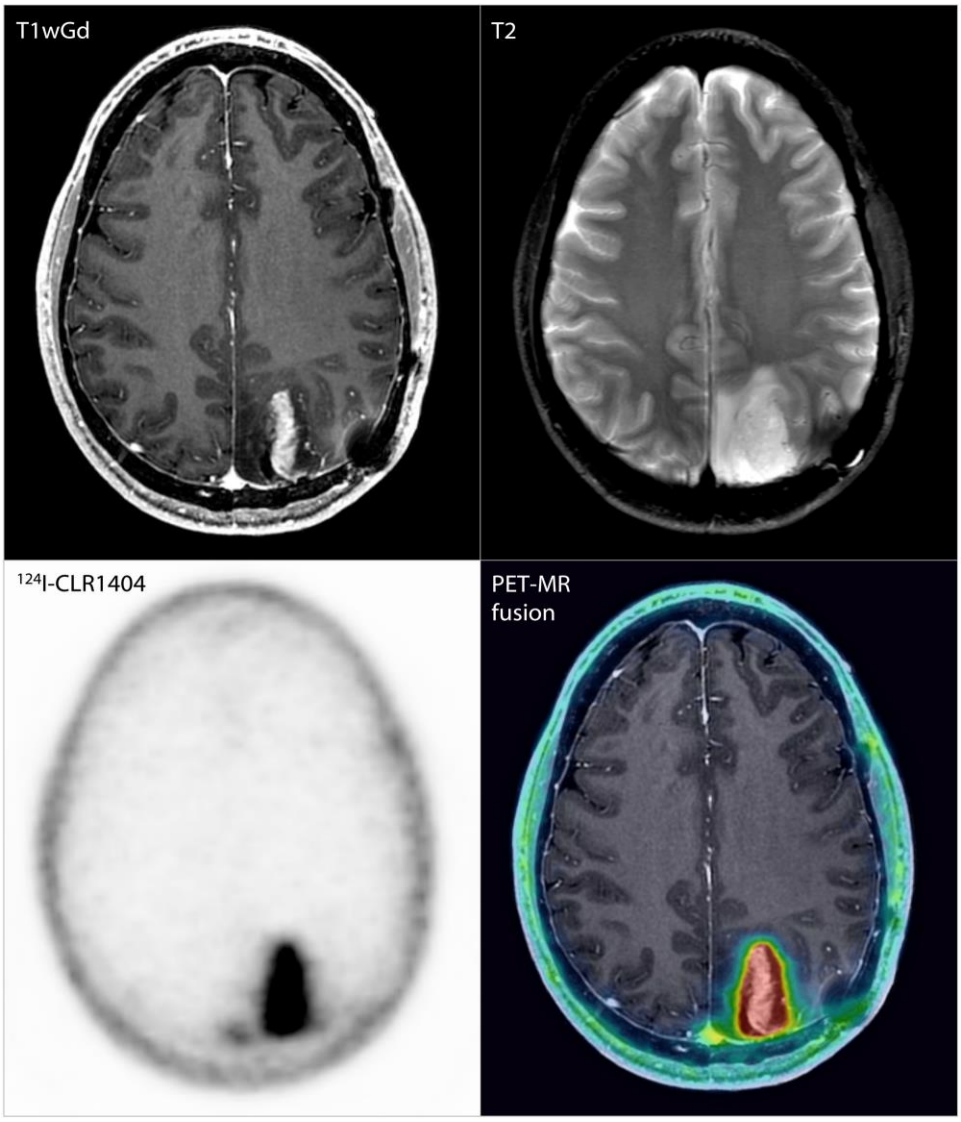

Figure S8. Recurrent WHO Grade III astrocytoma. Left parietal astrocytoma was resected 2 years before this axial T1-contrast MR and PET imaging that show likely recurrence. Fused PET-MRI is shown on the right.

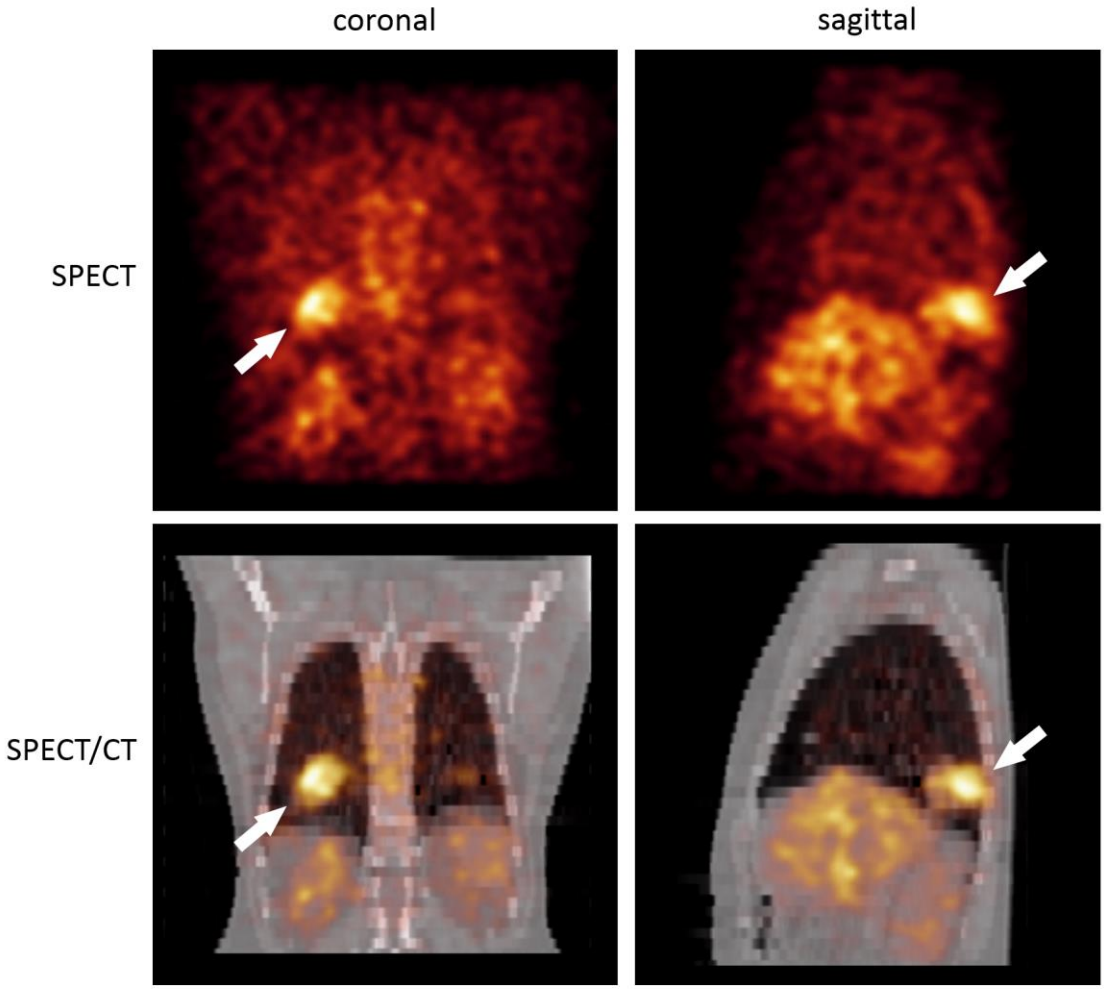

Figure S9. ^{131}I-CLR1404 SPECT/CT imaging of metastatic colorectal cancer. Coronal (**A**) and sagittal (**B**) SPECT images and corresponding fused SPECT/CT images (**C** and **D**) of a recurrent colorectal cancer patient with lung and liver metastases (arrow). Images obtained 21 days after injection of ^{131}I-CLR1404.

A

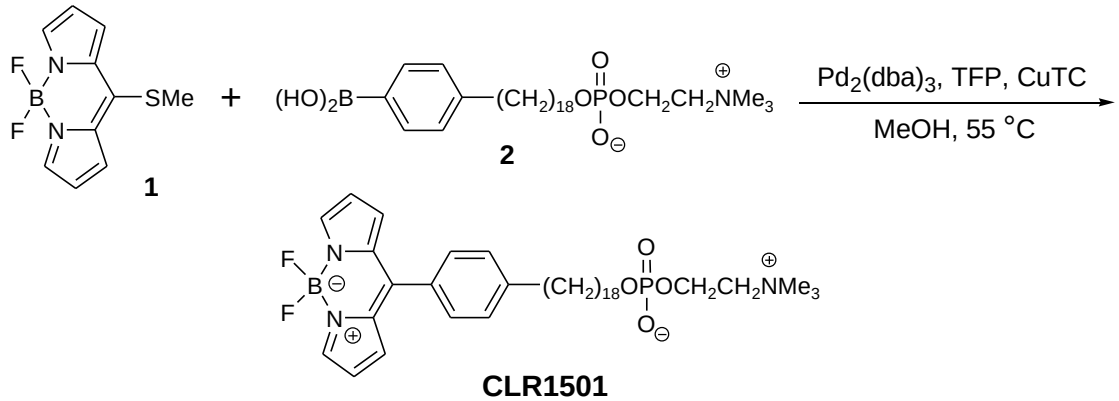

$Pd_2(dba)_3$ = tris-(dibenzylideneacetone) dipalladium (0)

TFP = tri-(2-furyl) phosphine = 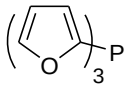

CuTC = copper (I) thiophene-2-carboxylate = 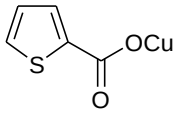

B

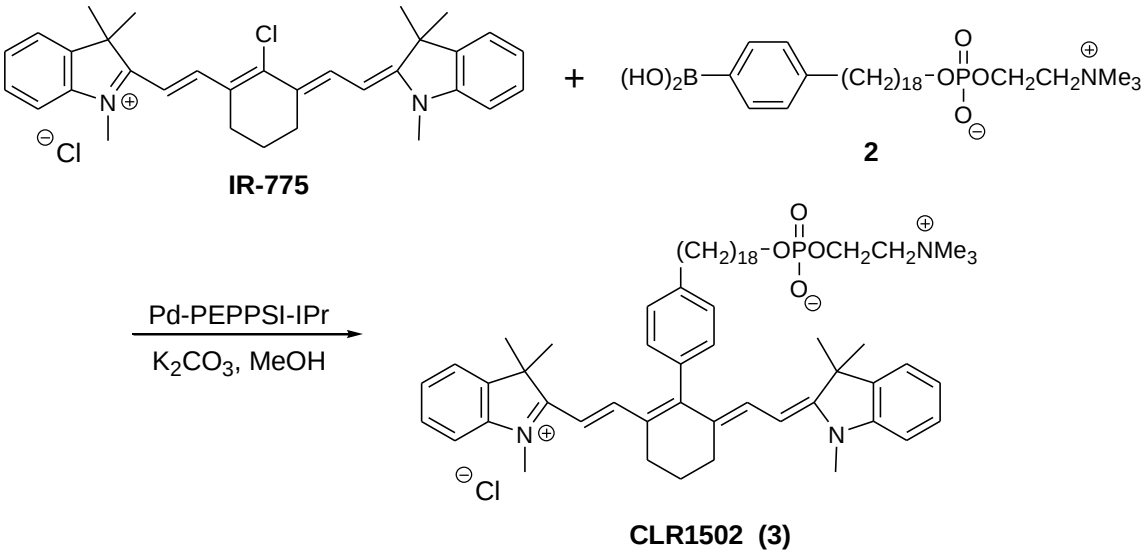

Figure S10. Synthesis of optical APC analogs. (**A**) Fluorescent analog CLR1501. (**B**) NIR analog CLR1502.

Supplementary Tables

Table S1: ^{124}I-CLR1404 uptake in tumor xenografts. Tumor uptake was considered positive if tumor to muscle ratio was > 3. Tumor:muscle ratio ≤ 2 was considered negative.

Tumor model		Species	Category	Tumor uptake[1]
1	Prostate PC-3	SCID mouse	Adenocarcinoma	Yes
2	Lung A-549 (NSCLC)	SCID mouse	Adenocarcinoma	Yes
3	Lung NCI H-69 (Oat Cell)	SCID mouse	Small cell carcinoma	Yes
4	Adrenal H-295	SCID mouse	Adenocarcinoma	Yes
5	Adrenal RL-251	SCID mouse	Adenocarcinoma	Yes
6	Colon-51	SCID mouse	Adenocarcinoma	Yes
7	Colon LS180	SCID mouse	Adenocarcinoma	Yes
8	Colon DLD1	SCID mouse	Adenocarcinoma	Yes
9	Colon HT-29	SCID mouse	Adenocarcinoma	Yes
10	Colon LS-180	Nude mouse	Adenocarcinoma	Yes
11	Glioblastoma U87	Nude mouse and NOD-SCID (orthotopic)	Glioma	Yes
12	Melanoma A-375	Nude mouse	Adenocarcinoma	Yes
13	Multiple myeloma MM.1S	Nude mouse	Myeloma	Yes
14	Neuroblastoma SK-N-AS	Nude mouse	Neuroblastoma	Yes
15	Neuroblastoma NB1691	Nude mouse	Neuroblastoma	Yes
16	Neuroblastoma CHLA-20	Nude mouse	Neuroblastoma	Yes
17	Neuroblastoma Lan5	Nude mouse	Neuroblastoma	Yes
18	Ovarian HTB-77	Nude mouse	Adenocarcinoma	Yes
19	Ovarian Ovcar-3	Nude mouse	Adenocarcinoma	Yes
20	Pancreatic BXPC3	Nude mouse	Adenocarcinoma	Yes
21	Pancreatic Mia Paca-2	Nude mouse	Carcinoma	Yes
22	Pancreatic Capan-1	Nude mouse	Adenocarcinoma	Yes
23	Renal cell Caki-2	Nude mouse (orthotopic)	Clear cell carcinoma	Yes
24	Renal cell ACHN	Nude mouse (orthotopic)	Adenocarcinoma	Yes
25	Sarcoma (Meth-A)	Nude mouse	Fibrosarcoma	Yes
26	Head and neck SCC1	Nude mouse	Squamous cell carcinoma	Yes
27	Head and neck SCC6	Nude mouse	Squamous cell carcinoma	Yes
28	Prostate LNCap	Mouse	Adenocarcinoma	Yes
29	Prostate LuCap	Mouse	Adenocarcinoma	Yes
30	Breast MCF-7	Rat	Adenocarcinoma	Yes
31	Triple negative breast	Nude mouse	Adenocarcinoma	Yes

	MDA-MB231			
32	Uterine MES SA/Dx5	Nude mouse	Sarcoma	Yes
33	Glioblastoma 22 GSC	NOD-SCID mouse (orthotopic)	Glioma	Yes
34	Glioblastoma 105 GSC	NOD-SCID mouse (orthotopic)	Glioma	Yes
35	Breast 4T1	Endogenous mouse (orthotopic)	Adenocarcinoma	Yes
36	Bladder SV40	Mouse (orthotopic)	Adenocarcinoma	Yes
37	Prostate MatLyLu	Rat	Adenocarcinoma	Yes
38	Walker256	Rat	Carcinosarcoma	Yes
39	TRAMP prostate	Endogenous mouse	Adenocarcinoma	Yes
40	Colon CT26	SCID mouse	Adenocarcinoma	Yes
41	Colon Pirc	Autochthonous Pirc rat	Adenocarcinoma	Yes
42	Min mouse intestinal	Endogenous mouse	Adenocarcinoma	Yes
43	Melanoma	Mouse	Adenocarcinoma	Yes
44	Mammary SCC	$Apc^{Min/+}$ mouse	Squamous cell carcinoma	Yes
45	Mammary AC	$Apc^{Min/+}$ mouse	Adenocarcinoma	Yes
46	Hepatocellular carcinoma	Endogenous mouse	Adenocarcinoma	Yes
47	Glioma L9	Rat xenograft	Glioma	Yes
48	Glioma C6	Rat xenograft	Glioma	Yes
49	Glioma CNS1	Rat xenograft	Glioma	Yes
50	Glioma RG2	Rat xenograft	Glioma	Yes
51	Retinoblastoma	Endogenous mouse	Blastoma	Yes
52	Pancreatic c-myc	Endogenous mouse	Adenocarcinoma	Yes
53	Pancreatic Kras	Endogenous mouse	Adenocarcinoma	Yes
54	Cervical-HPV	Endogenous mouse	Adenocarcinoma	Yes
55	Esophageal	Endogenous Mouse	Adenocarcinoma	Yes
1	Intestinal polyp	Endogenous mouse	Adenoma (benign)	No
2	Mammary alveolar hyperplasia	Endogenous mouse	Hyperplasia (benign)	No
3	Hepatoma Hep-3B	Nude mouse	Carcinoma	No
4	Hepatoma Hep-G2	Nude mouse	Carcinoma	No
5	Pirc rat colon adenoma	Pirc rat	Adenoma	No

SUPPLEMENTARY VIDEOS

Movie S1. Cellular uptake of CLR1501 in prostate cancer cells. PC3 (human prostate adenocarcinoma), was stained with MitoTracker Red CMXRos dye and blue-fluorescent Hoechst 33342 dye for mitochondrial and nuclear imaging, respectively. Image acquisition started upon adding 5 μM CLR1501 *in vitro* and continued for 1 hour.

Movie S2. Dual modality PET/CT virtual colonoscopy in Pirc model. Endoluminal fly through of rat colon showing premalignant adenomas (yellow masses) and one malignant adenocarcinoma (red mass).